

Performance evaluation of the RYSEN:
a 3D overground body weight
support system

Robert J. Peuchen

Performance evaluation of the RYSEN: a 3D overground body weight support system

by

Robert J. Peuchen

to obtain the degree of

Master of Science

in Mechanical Engineering

at Delft University of Technology,

to be defended publicly on Friday April 20, 2018 at 10:00 AM.

Student number: 4172787
Thesis committee: Prof. dr. ir. Heike Vallery, TU Delft, Biorobotics, *supervisor* (Chair)
dr. ir. Michiel Plooij, TU Delft - Motek Medical B.V., *supervisor*
Prof. dr. ir. Martijn Wisse, TU Delft, Cognitive Robotics

This report cannot be made public until April, 2023.

Abstract

Body weight support (BWS) systems are widely used in gait rehabilitation. These systems allow patients to gradually increase training intensity and promote independent walking. Currently, there is no standardized method to assess the performance of BWS systems. This work proposes methods and metrics that can be used to assess and compare any overground, force controlled BWS systems. The RYSEN, a novel, cable-driven, three-dimensional overground BWS system, developed by Motek Medical B.V., Delft University of Technology, GTX Medical and École Polytechnique Fédérale de Lausanne, is used as a case study throughout this work.

Analytical methods are proposed that allow to (1) define the non-linearity bounds of static spring systems and (2) select the most important configurations for performance evaluation using sensitivity analyses on weighted stiffness matrices. These analytical methods resulted in testing the system in one direction at a time for a limited number of configurations. Furthermore, experiments are proposed based on three modes of operation: static force tracking, sinusoidal force tracking and disturbance rejection. The input signals for these experiments are based on human walking and support strategies. A test setup, equipped with an external sensor and reciprocal mechanism, was used to objectively obtain the frequency response, tracking and estimation error of the RYSEN. The experiments were successful in characterizing the RYSEN in the chosen configurations. This showed that currently the force estimation is the main limitation of performance. The experiments will be repeated with minor adjustments to the test setup and using improved hardware in the RYSEN.

Symbols

Symbol	Description	First occurrence
x, y, z	Position or direction	Ch. 1
$f(x)$	Function with general input x	Sec. 2.2.1
ϵ_l	Model linearization error	Sec. 2.2.1
\mathbf{J}	Jacobian matrix	Sec. 2.2.1
\mathbf{C}	Configuration	Sec. 2.2.2
\mathbf{P}^*	Desired position vector	Sec. 2.2.2
x_r, y_r, z_r	Desired position	Sec. 2.2.2
\mathbf{F}^*	Desired unloading force	Sec. 2.2.2
\mathbf{V}	Position disturbance vector	Sec. 2.2.2
i	Direction of force/position	Sec. 2.2.2
δ_i	Position disturbance	Sec. 2.2.2
F_i	Force at endpoint	Sec. 2.2.2
Y_i	Output/cost function	Sec. 2.4.1
η_i	Linearization error bounds	Sec. 2.4.1
k	Stiffness (spring)	Sec. 2.4.2
w	Width of the Rysen	Sec. 2.4.2
L_0	Spring zero rest length	Sec. 2.5.2
θ	Angle in models	Sec. 2.5.3
L	Length	Sec. 2.5.3
ϵ_t	Tracking error	Sec. 3.2.1
\mathbf{X}	Position vector	Sec. 3.2.1
\mathbf{k}	Stiffness matrix	Sec. 3.2.1
$k_{i,j}$	Element of stiffness matrix	Sec. 3.2.1
M_0	Moment around base	Sec. 3.2.3
W_n	Weight factor stiffness matrix	Sec. 3.2.3
Δ	Difference in input parameter	Sec. 3.3.1
S_p	First-order indices	Sec. 3.3.3
$S_{p,q}$	Higher-order indices	Sec. 3.3.3
$S_{T,p}$	Total-effect indices	Sec. 3.3.3
m	Mass (CPS)	Sec. 3.5.4
\dot{y}, \ddot{y}	Velocity/acceleration (CPS)	Sec. 3.5.4
H	Transfer function	Sec. 3.5.4
ϵ_{est}	Estimation error	Sec. 4.2.2
f	Frequency step	Sec. 4.4
O	Force offset	Sec. 4.7
ϕ	Phase shift	Sec. 4.7
G	Gain	Sec. 4.7
F_R	Force estimation Rysen	Sec. 5.3

Abbreviations

Abbreviation	Definition	First occurrence
BWS	Body weight support	Ch. 1
SCI	Spinal cord injury	Ch. 1
CoP	Centre of pressure	Ch. 1
CDPM	Cable-driven parallel mechanism	Ch. 1
IMU	Inertial measurement unit	Ch. 1
CPS	Central point of suspension	Ch. 1
VR	Variable-radius	Ch. 1
CoM	Centre of mass	Ch. 1
OAT	One (direction) at a time	Ch. 1
BWU	Body weight unloading	Sec. 2.2.2
DoF	Degree of freedom	Sec. 2.5.4
SA	Sensitivity analysis	Sec. 3.1
BoS	Base of support	Sec. 3.2.3
LSA	Local sensitivity analysis	Sec. 3.3.1
LS	Local sensitivity	Sec. 3.3.1
GSA	Global sensitivity analysis	Sec. 3.3.2
EET	Elementary effect size	Sec. 3.3.2
VBSA	Variance-based sensitivity analysis	Sec. 3.3.2
FAST	Fourier amplitude sensitivity test	Sec. 3.3.2
RMS	Root mean square	Sec. 4.2.2

Contents

1	Introduction	1
2	Methods I - Linearity of body weight support systems	5
2.1	Overview	5
2.2	Linear approximation	5
2.2.1	General equations	5
2.2.2	Disturbance-in, force-out systems	6
2.3	Metrics	7
2.4	Linearization criteria	7
2.4.1	Bounds of non-linearity	7
2.4.2	Selected disturbances and parameters	7
2.5	Selected non-linear models	8
2.5.1	Types of models	8
2.5.2	1D non-linear model	8
2.5.3	2D non-linear model	8
2.5.4	Parallel model	10
2.6	Results	11
2.6.1	1D non-linear model results	11
2.6.2	2D non-linear model results	11
2.6.3	Parallel model results	11
2.7	Discussion	12
2.7.1	Threshold of non-linearity	12
2.7.2	The influence of force modulation on linearity	13
2.8	Conclusion	13
3	Methods II - Configuration selection for RYSEN evaluation	15
3.1	Overview	15
3.2	Selected metrics and weight factors	15
3.2.1	Metrics	15
3.2.2	Stiffness ellipsoids	16
3.2.3	Assessing the elements of the stiffness matrix	16
3.3	Sensitivity analysis	18
3.3.1	Local sensitivity analysis	18
3.3.2	Global sensitivity analysis	19
3.3.3	Variance-based sensitivity analysis	19
3.3.4	VBSA sampling approach	20
3.4	Results	20
3.5	Discussion	20
3.5.1	Level of complexity	20
3.5.2	From VBSA results to experiments	21
3.5.3	Model simplification	21
3.5.4	Connection to harness	21
3.6	Conclusion	22
4	Methods III - Experimental evaluation of body weight support systems	23
4.1	Overview	23
4.2	Experiments, metrics and configurations	23
4.2.1	Experiments	23
4.2.2	Metrics	23
4.2.3	Configurations	24

4.3	Static force tracking	25
4.4	Force output performance	25
4.5	Disturbance rejection performance or 'zero-impedance mode'	25
4.6	Test setup	25
4.7	Data processing	26
4.8	Conclusion	27
5	Results - Performance of RYSEN	29
5.1	Overview	29
5.2	Initial observations	29
5.3	Static force estimate performance	30
5.4	Output force performance	30
5.4.1	Notes on the 'dynamic' experiments	30
5.4.2	Output force performance: x-direction	30
5.4.3	Output force performance: y-direction.	31
5.4.4	Output force performance: z-direction	31
5.5	Disturbance rejection performance	33
5.5.1	Disturbance rejection performance: x-direction	33
5.5.2	Disturbance rejection performance: y-direction	34
5.5.3	Disturbance rejection performance: z-direction	36
5.6	Nominal cases: overview	37
5.7	Non-nominal cases: overview.	38
5.8	Discussion	38
5.8.1	Dominant behaviour.	38
5.8.2	Test improvements.	38
5.9	Conclusion	39
6	Summary of discussions	41
6.1	Overview	41
6.2	Analytical methods	41
6.3	Experimental methods	42
6.4	Contributions to the field of performance evaluation	42
7	Conclusions	43
	Bibliography	45
A	Appendix: Variance-based sensitivity analysis	47
B	Appendix: Test protocol	49
B.1	Protocol and safety during the experiments.	49
B.1.1	Protocol	49
B.1.2	Checks in-between tests	49
C	Appendix: Additional figures	51
C.1	Force output experiment: non-nominal cases	51
C.2	Disturbance rejection experiment: non-nominal cases	54



Introduction

Body weight support (BWS) systems are useful in the rehabilitation of severe gait impairments such as stroke [1, 2] and spinal cord injury [3, 4]. BWS systems carry part of the subject's body weight and help to gradually increase training intensity. With BWS systems, the subject is still being able to move independently. The required physical assistance by a therapist is minimized. BWS systems can be categorized as treadmill-based and overground systems. Treadmill-based systems generally have a one-dimensional attachment point above a treadmill, either passive or actively modulated. The major disadvantage of treadmill-based systems is that the muscle activation patterns, joint moments and powers are different from overground walking [5, 6]. This can arguably result in changes of locomotion strategy and gives the training environment a lower fidelity with respect to actual walking. For overground BWS systems the point of support moves along with the subject, while walking on a stationary surface, resembling a normal walking environment.

Recently, Mignardot et al. [4] showed that a combination of vertical and horizontal support forces may improve the recovery of spinal cord injury (SCI) patients using an overground BWS system. When applying vertical forces, the centre of pressure (CoP) of the patient shifts toward the heels. This can result in abnormal gait in patients, which in turn can result in learning an incorrect gait. The change of CoP location can be counteracted by simultaneously applying horizontal forces to the patient. The RYSEN is a novel body weight support system that follows a patient and can provide this combination of vertical and horizontal support forces during walking.

The RYSEN (Fig. 1.1) is a cable-driven, multi-directional overground body weight support system is developed by Motek Medical B.V., in collaboration with Delft University of Technology, GTX Medical and the Centre for Neuroprosthetics at École Polytechnique Fédérale de Lausanne [7]. Unlike most BWS systems, RYSEN allows free motion and support forces in three-dimensions over a large workspace. This way, various exercises such as stair climbing and interactive games can be facilitated. The use of cables also allow for a low inertia, reconfigurability and dynamic manoeuvrability, while retaining simplicity, as applicable to the class of cable-driven parallel mechanisms (CDPM) [8, 9]. The main actuated components of the RYSEN are two winches, a single variable-radius winch and two pairs of trolleys to provide the vertical, lateral and forward motions respectively. The device is connected at the central point of suspension (CPS) to the subject through the slingbar and harness. The location of the CPS is estimated based on motor positions and acceleration (IMU) data from the slingbar. Cable forces are measured through one-dimensional force sensors. The combination of CPS location and cable forces give an estimate of the forces at the CPS, thus the support forces of the device on the subject.

Performance evaluation is an essential step in system development. The results are important to various stakeholders such as subjects, clients, researchers and insurance companies. Performance evaluation also allows objective comparison of system characteristics with other BWS systems. Currently, there is no such standardized performance evaluation protocol for BWS systems. Therefore, this work is about the performance evaluation of the RYSEN and other BWS systems.

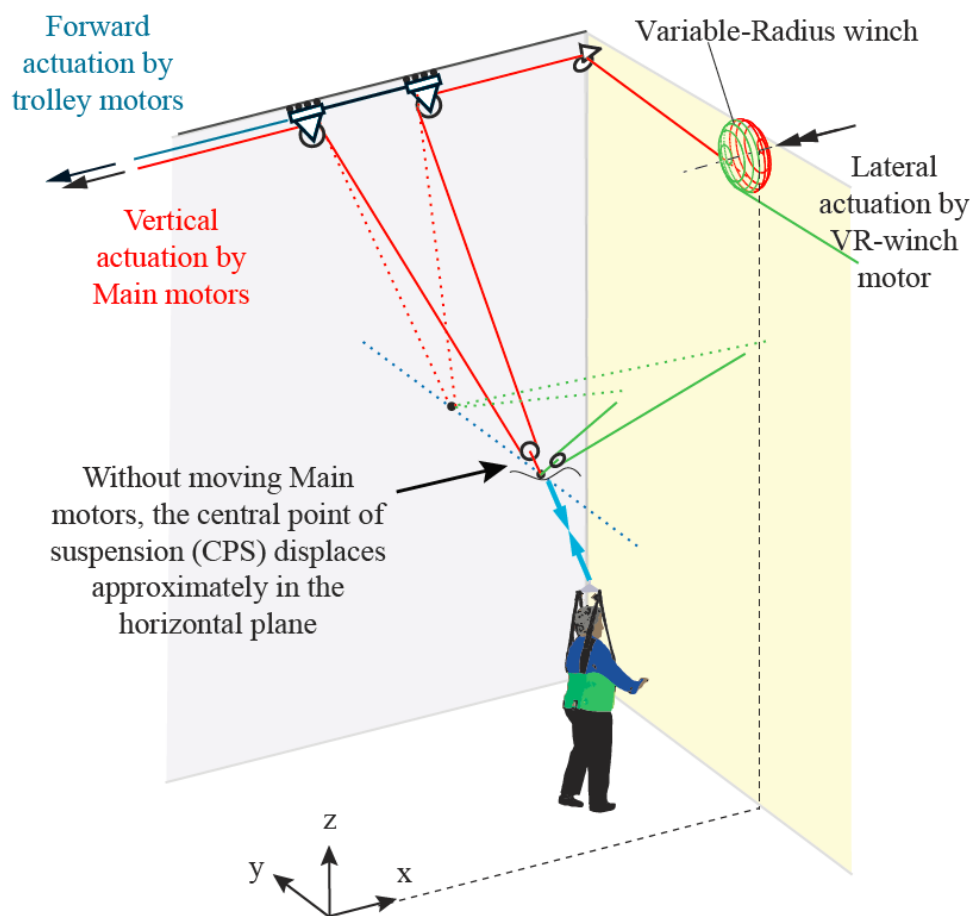
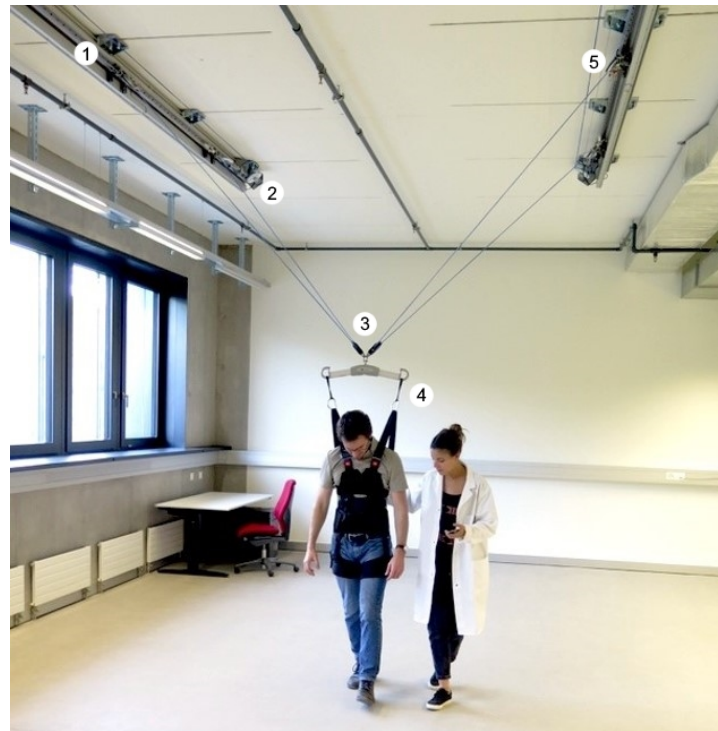


Figure 1.1: (a) RYSEN in action. The identifiers represent the rails (1), cable force sensing (2), central point of suspension (CPS) (3), slingbar and harness (4) and pair of trolleys (5). Used with permission from Motek Medical B.V. (b) Schematic overview of the working principle of the RYSEN [7]. Used with permission from the authors.

A companion report summarises published work on metrics, analysis and experimental methods used in the performance evaluation of CDPM and BWS systems [10]. This report identified the most commonly used metrics: transparency or task distortion, force bandwidth, disturbance (rejection) bandwidth and displacement capabilities. A large number of studies also analytically determined the workspace and the optimization thereof. The wrench-feasible workspace [11, 12] was identified as the most frequently used metric for determining the analytical workspace. In validation experiments, less consistency was observed in the performance evaluation of CDPM and BWS systems. Published experiments are mostly for demonstrative purposes, showing the performance for one condition and one task. This makes it difficult to objectively compare devices that perform slightly different tasks. Furthermore, most studies make use of the device's own sensors to determine the tracking capabilities of either force or position. To remove bias in performance evaluation, experimental test setups need to be designed to systematically assess the selected metrics and parameters.

The most notable systematic validation studies of cable-driven BWS validation are those of Hidler et al. [13] for the ZeroG, and Bannwart et al. [14] for the FLOAT. Hidler et al. used a range of loads and disturbing frequencies to check the constant force tracking performance i.e. transparency. However, their study made use of ZeroG's own force sensors for tracking, introducing a bias when this force is being modulated by the system. Bannwart et al. used an external force sensor and linear actuator to systematically validate system performance in static and dynamic cases. However, their study did not evaluate performance for the small, fast perturbations induced by the motion of the center of mass (CoM) of a human [15, 16]. Moreover, the influence of workspace location was not addressed in the study of Bannwart et al. Workspace location can possibly change the characteristics and performance of the device, as is the case in CDPM with fixed actuator locations [17].

This work determines the relevant experiments for BWS systems and its validity to describe the system's complete performance. Standardized methods and metrics are introduced to test the performance of BWS systems for relevant parameters and disturbances. The selected experiments are performed and the results are visualized and evaluated for the RYSEN as a case study. Three main challenges have to be addressed when designing experiments for systematic performance evaluation and mimicking realistic perturbations of a subject:

1. excitation of the endpoint
2. selecting possible configurations
3. visualization of results

First, when using an external test setup, the system is usually perturbed in one direction at a time (OAT). This is not a problem for linear systems, as the principle of superposition allows for system outputs to be added to give an estimate of the total performance. However, when dealing with non-linear systems such as the RYSEN, it must be determined if superposition holds to a reasonable degree for the sum of perturbations. If not, a more complex device is needed to mimic the simultaneous perturbations given by a subject. Secondly, there are many configurations that can influence performance, such as unloading force, workspace location, amplitude and frequency of perturbation. It is useful to limit the number of configurations and combinations beforehand. Sensitivity analysis is used to identify the configurations that influence system performance. Finally, the visualization of performance metrics and parameter influence is limited in current literature. Novel ways of visualizing the metrics are needed to more clearly showcase system performance. This will likely promote acceptance of novel systems by stakeholders.

In Chapter 2, the linearity of static spring systems, representing BWS systems, will be examined over the range of configurations. This will determine if a one-dimensional test setup can be used for the complete performance evaluation of the RYSEN. Chapter 3 will select the most important configurations, based on sensitivity analysis of system characteristics. This will select the configurations that will be tested in the experiments. In Chapter 4, the required experiments and test setup are introduced, which are recommended to evaluate any BWS system. The remaining chapters will evaluate the results, identify limitations and possible improvements for the RYSEN and reflect on the chosen methods.

2

Methods I - Linearity of body weight support systems

2.1. Overview

During gait, subjects give oscillatory perturbations in three directions to the endpoint of body weight support (BWS) systems. Most notable are the vertical and lateral perturbations. Ideally, for objective performance evaluation, an external test setup would mimic the disturbance of a subject on the system and measure the resulting interaction forces (i.e. transparency) [10, 18]. However, an expensive and bulky test setup would be required to mimic these perturbations simultaneously.

Linear systems can be tested for one direction at a time (OAT), with the output responses to be added based on the principle of superposition. When testing non-linear systems for OAT, the degree of non-linearity will induce an estimation error of total performance when examining tracking errors of separate tests. See Figure 2.1 on how the linearization error adds to the uncertainty of the tracking error or interaction forces.

In this chapter, metrics are proposed to estimate the linearization error of non-linear systems. The goal is to determine whether BWS systems can be tested in one direction at a time and what the linearization error could be if these separate responses are added. Several simplified spring models representing BWS systems are analyzed for the configuration space and perturbations of human walking.

First an introduction to model approximation and linearization will be given. Then a set of proposed metrics and analyses are introduced. Three models, representing BWS systems, will be assessed for the error between the linearized and actual system. Results will show the degree of non-linearity for small perturbations on static spring systems. The limits of this linearization error are task and system dependent. It is speculated that these errors are low enough to use a simplified test setup that evaluates in OAT within a range of uncertainty. Finally, it is discussed how actuated systems and the quality thereof will influence the linearization error for larger perturbations, such as overground walking or forward movement in the RYSEN.

2.2. Linear approximation

2.2.1. General equations

Non-linear systems can be approximated using system linearization. In this case, the linearization error is determined as the error that could occur when testing a system in one direction at a time (OAT) and adding the separate responses.

In general, the system output can be described as the linear approximation (f_l) and the accompanying linearization error (ϵ_l). The linear approximation in configuration point C is described as follows:

$$\begin{aligned} f(x) &= f_l(x) + \epsilon_l \\ f_l(x) &= f(C) + \nabla f|_C \cdot (x - C) \end{aligned} \quad (2.1)$$

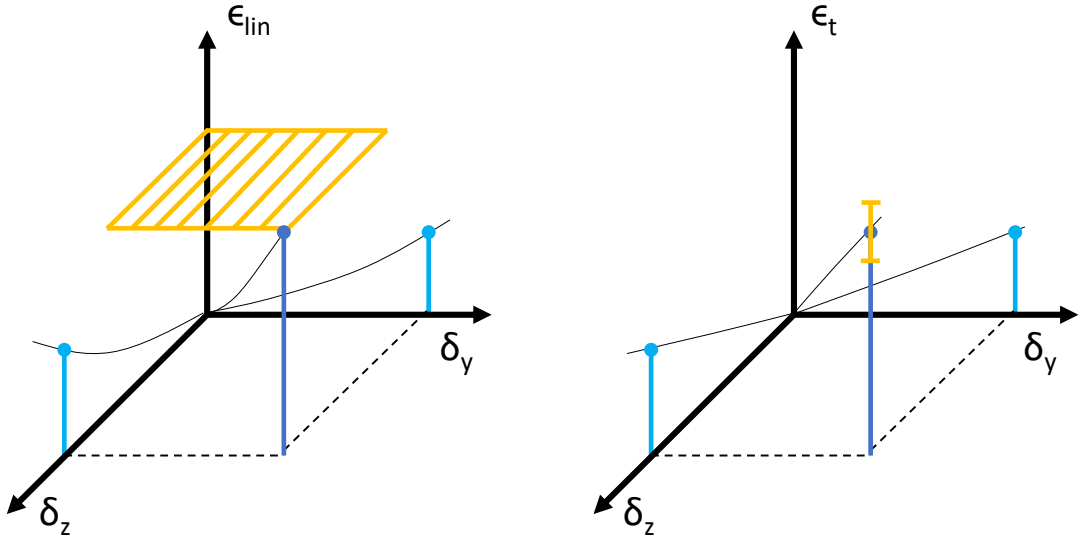


Figure 2.1: Overview of the linearization error (ϵ_l) with respect to the tracking error (ϵ_t): the uncertainty of perturbing a non-linear system in one direction at a time (OAT) is shown in yellow. This is a (conservative) measure of non-linearity, introduced in this chapter.

where $\nabla f|_C$ is the gradient of f in configuration point C for general input variables x . In the case of multiple inputs, the gradient of the variables on the output is often shown using the Jacobian matrix \mathbf{J} :

$$\mathbf{f}_l(x) = \mathbf{f}(C) + \mathbf{J}(C)(x - C) \quad (2.2)$$

with

$$\mathbf{J} = \begin{bmatrix} \frac{\partial f_1}{\partial x_1} & \cdots & \frac{\partial f_1}{\partial x_n} \\ \vdots & \ddots & \vdots \\ \frac{\partial f_m}{\partial x_1} & \cdots & \frac{\partial f_m}{\partial x_n} \end{bmatrix}$$

2.2.2. Disturbance-in, force-out systems

This chapter evaluates models with input position disturbances and output force. These models represent static BWS systems subjected to disturbances. The axes are chosen such that they correspond with the axes of the RYSEN (Fig. 1.1). The configuration C and disturbance V are chosen as input values of the system, for which the system is linearized. For the case of a 2D system:

$$\begin{aligned} \mathbf{C} &= [\mathbf{P}^*, \mathbf{F}^*]^T \\ \mathbf{P}^* &= [y_r, z_r]^T \\ \mathbf{F}^* &= [F_y^*, F_z^*]^T \\ \mathbf{V} &= [\delta_y, \delta_z]^T \end{aligned}$$

where y_r, z_r represent the configuration rest positions, F_y^*, F_z^* the required body weight unloading (BWU) vector and δ_y, δ_z the disturbance in y - and z directions respectively. The system can then be described as a linear system and its linearization error (ϵ_l):

$$F_i(\mathbf{C}, \mathbf{V}) = F_i(\mathbf{C}, 0) + \frac{\partial F_i(\mathbf{C}, 0)}{\partial y} \delta_y + \frac{\partial F_i(\mathbf{C}, 0)}{\partial z} \delta_z + \epsilon_{l,i} \quad (2.3)$$

where F_i is the force in direction i and $(\mathbf{C}, 0)$ the rest configuration. The partial derivatives are simply the elements of the stiffness matrix that can be encompassed again by the Jacobian matrix ($\mathbf{J}(\mathbf{C}, 0)$).

$$\mathbf{F}(\mathbf{C}, \mathbf{V}) = \mathbf{F}(\mathbf{C}, 0) + \mathbf{J}(\mathbf{C}, 0)\mathbf{V} + \boldsymbol{\epsilon}_l \quad (2.4)$$

with

$$\mathbf{F} = \begin{bmatrix} F_y \\ F_z \end{bmatrix}$$

$$\mathbf{J} = \begin{bmatrix} \frac{\partial F_y}{\partial y} & \frac{\partial F_y}{\partial z} \\ \frac{\partial F_z}{\partial y} & \frac{\partial F_z}{\partial z} \end{bmatrix}$$

2.3. Metrics

Metrics are needed to assess the non-linearity of a system and the error induced when testing in one direction at a time (OAT). The assessment allows estimating the total possible error when adding outputs for a set of disturbances in a certain location. This error can be regarded as an absolute error (N) or a relative error (-).

The absolute linearization error:

$$\epsilon_{l,i} = F_i(\mathbf{C}, \mathbf{V}) - F_{l,i}(\mathbf{C}, \mathbf{V}) \quad (2.5)$$

$$|\epsilon_{\text{tot}}| = \sqrt{\epsilon_{l,1}^2 + \dots + \epsilon_{l,i}^2} \quad (2.6)$$

The relative- or normalized linearization error:

$$\left(\frac{\epsilon_l}{F}\right)_i = \frac{\epsilon_{l,i}}{F_i(\mathbf{C}, \mathbf{V})} \quad (2.7)$$

$$\left|\frac{\epsilon}{F}\right|_{\text{tot}} = \frac{|\epsilon_{\text{tot}}|}{\sqrt{F_1^2 + \dots + F_i^2}} \quad (2.8)$$

2.4. Linearization criteria

2.4.1. Bounds of non-linearity

The absolute and relative linearization error can be mapped with respect to the configuration: the desired position and unloading force. To determine if the bounds of non-linearity are acceptable, only the maximum values are determined and chosen as the metric of evaluation:

$$Y_1 = \max(|\epsilon_{\text{tot}}|) = \max(f(\mathbf{C}, \mathbf{V})) \leq \eta_1 \quad (2.9)$$

$$Y_2 = \max\left(\left|\frac{\epsilon}{F}\right|_{\text{tot}}\right) = \max(f(\mathbf{C}, \mathbf{V})) \leq \eta_2 \quad (2.10)$$

where η_i is a self-defined bound on the absolute or relative linearization error. This means that every configuration gives a maximum uncertainty of η_i when adding two disturbances and assuming superposition on the output. The configuration and disturbance parameters should be bounded in order to find the maximum values of the linearization error. Finding this maximum value gives a conservative measure for the non-linearity in the system. This report does not address acceptance of η_i i.e. when the value of η_i is "too high".

2.4.2. Selected disturbances and parameters

Configuration and disturbance parameters are selected based on real BWS systems [13, 19], common BWU configurations [20] and CoM motion in human walking [15, 16]. The body weight of a subject is assumed to be 75 kg [21]. The results of Y_i are ultimately shown for each configuration, such that they give the bounds η_i for each configuration point.

Table 2.1: System parameters, disturbance- and configuration ranges used to determine the maximum linearization errors.

Parameter	Min. value	Max. value	Nominal value	Units
k	-	-	5000	N/m
w	-	-	3	m
δ_y	± 0.015	± 0.035	-	m
δ_z	± 0.0138	± 0.0245	-	m
y_r	0.5	2.5	1.5	m
z_r	-1	-3	-2	m
F_z^*	15	60	30	%

2.5. Selected non-linear models

2.5.1. Types of models

The disturbance-in, force-out models are selected based on increasing complexity and resemble existing BWS systems. Figure 2.2 gives an overview of the n-dimensional non-linear models.

2.5.2. 1D non-linear model

The 1D spring system, Fig. 2.2a, consists of a single non-linear spring. Its rest length is determined by the unloading force (F^*) and rest position (z_r).

$$L_0 = -z_r - \sqrt{\frac{F^*}{k}} \quad (2.11)$$

$$F(z) = k(-z - L_0)^2 = k\left(-z + z_r + \sqrt{\frac{F^*}{k}}\right)^2 \quad (2.12)$$

where k is the spring stiffness constant, L_0 the rest length and z the actual position. For a perturbation (δ) from the rest position the force is:

$$F(z_r + \delta) = k\left(-\delta + \sqrt{\frac{F^*}{k}}\right)^2$$

In this representation, $\delta = 0$ gives $F = F^*$. The linearized system, from the rest position, is given as:

$$F_l(\delta) = F^* + \left. \frac{\partial F}{\partial z} \right|_{z_r} \delta = F^* - 2k\delta \sqrt{\frac{F^*}{k}} \quad (2.13)$$

The absolute and relative linearization errors are then calculated as:

$$\begin{aligned} \epsilon &= F(z_r + \delta) - F_l(\delta) \\ \epsilon &= k\delta^2 \end{aligned} \quad (2.14)$$

$$\left(\frac{\epsilon}{F(z_r + \delta)} \right) = \frac{\delta^2}{\left(-\delta + \sqrt{\frac{F^*}{k}}\right)^2} \quad (2.15)$$

This shows that the absolute error of this model is proportional to the spring stiffness and quadratic to the magnitude of perturbation. This indicates that the largest linearization error is found at the maximum bounded disturbance. The unloading force only influences the relative error.

2.5.3. 2D non-linear model

The 2D spring system incorporates a linear spring and two directions of disturbance, as shown in Figure 2.2b. This means that the combination of y/z-position is non-linear. This model can be regarded as a simplified version of the Zero-G [13], which has a single point of suspension. The angle and length are determined using the geometry of the system:

$$\begin{aligned} \theta &= \tan^{-1}\left(\frac{y}{-z}\right) \\ L &= \frac{y}{\sin(\theta)} \end{aligned}$$

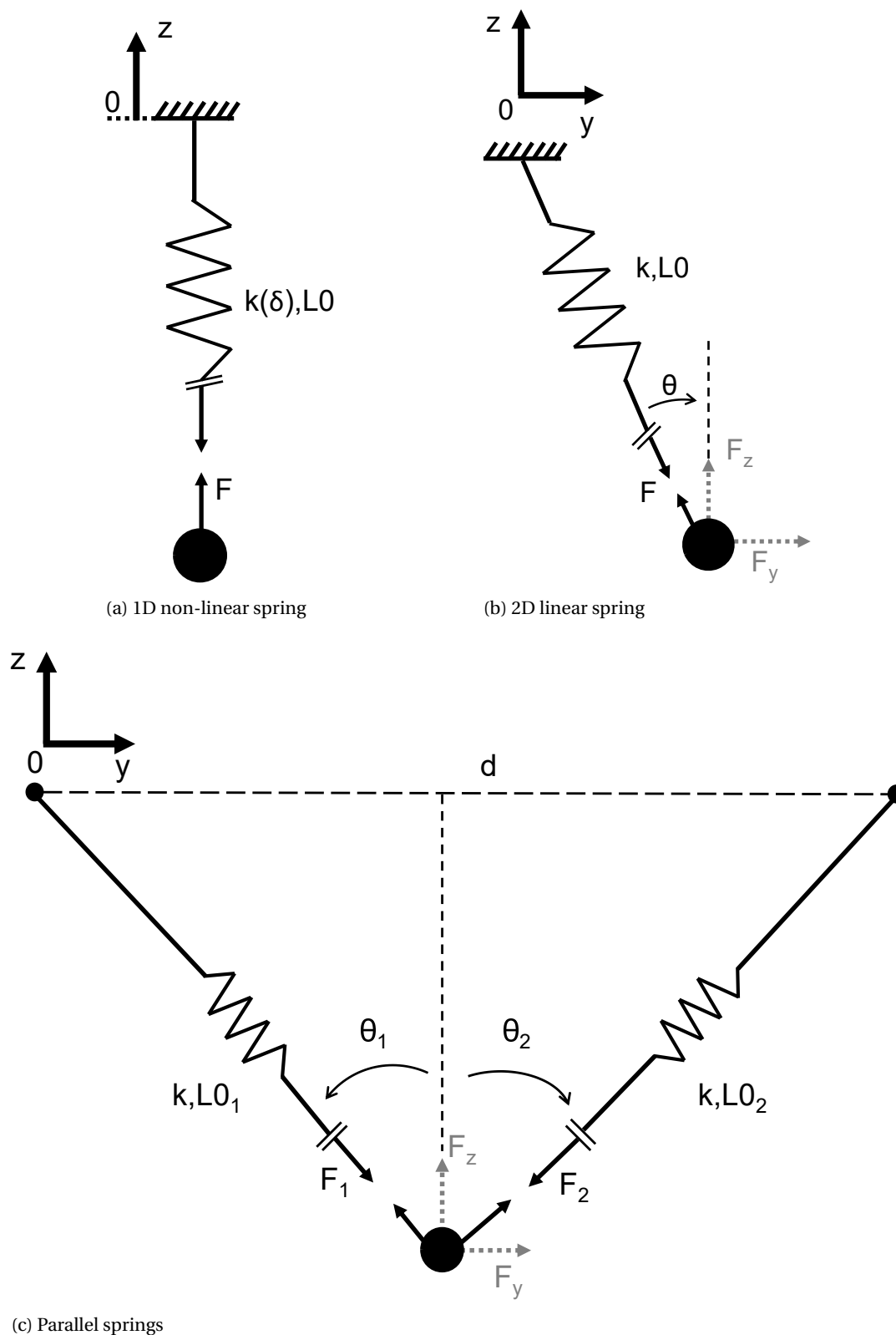


Figure 2.2: Spring models used in non-linearity analysis: (a) 1D spring system consisting of a single non-linear spring. (b) 2D spring system including a linear spring, resembling a simplified version of the Zero-G [13], neglecting the forward motion. (c) 2D parallel spring system, containing linear springs, resembling a simplified version of the RYSEN [7], neglecting the forward motion.

The rest length and force of the spring are then determined by position, stiffness (k), the rest position (z_r) and unloading force (F^*).

$$L_0 = -z_r - \frac{F^*}{k} \quad (2.16)$$

$$F = k(L - L_0) \quad (2.17)$$

The decomposition of forces can be derived from the geometry of the system.

$$F_y = -F \sin(\theta)$$

$$F_z = F \cos(\theta)$$

The linearized forces can then be determined with 2.3, resulting in:

$$F_{l,y} = \frac{F^* \delta_y}{z_r} \quad (2.18)$$

$$F_{l,z} = F^* - \delta_z k \quad (2.19)$$

The absolute- and relative linearization error from the y- and z-direction are then derived from Equations 2.6 and 2.8 respectively.

2.5.4. Parallel model

Figure 2.2c shows a simplified model representing the RYSEN. In this model, the motion in x-direction is neglected. This degree of freedom (DoF) is accounted for by the trolley movement in the real system. This x-location also does not change the stiffness characteristics of the system. Finally, the stiffness in x-direction is lower for small disturbances due to the passive pulleys connected to the CPS.

The model consists of two springs in parallel connected at the endpoint. The springs are separated by width w on the other end. The endpoint can be configured (C) for position (y_r, z_r) and unloading force (F_y^*, F_z^*). First, the geometry is used to determine the directional forces on the endpoint.

$$\theta_1 = \tan^{-1}\left(\frac{y}{-z}\right), \quad \theta_2 = \tan^{-1}\left(\frac{w-y}{-z}\right)$$

which also determine the total lengths of the springs.

$$L_1 = \frac{y}{\sin(\theta_1)}, \quad L_2 = \frac{w-y}{\sin(\theta_2)}$$

The forces in the cables are calculated as follows:

$$F_1 = k(L_1 - L_{0,1}), \quad F_2 = k(L_2 - L_{0,2})$$

The projected forces in y- and z-direction are:

$$F_y = F_{1,y} + F_{2,y} = -F_1 \sin(\theta_1) + F_2 \sin(\theta_2)$$

$$F_z = F_{1,z} + F_{2,z} = F_1 \cos(\theta_1) + F_2 \cos(\theta_2)$$

The zero-force lengths $L_{0,i}$ of the springs are symbolically solved based on the initial configuration C with the following known conditions:

$$F_y = F_y^*, \quad F_z = F_z^*$$

$$y = y_r, \quad z = z_r$$

giving:

$$L_{0,1} = - \frac{\sqrt{\frac{y_r^2}{z_r^2} + 1} (F_z^* w - F_z^* y_r + F_y^* z_r + w k z_r)}{k w} \quad (2.20)$$

$$L_{0,2} = - \frac{\sqrt{\frac{(w-y_r)^2}{z_r^2} + 1} (F_z^* y_r - F_y^* z_r + w k z_r)}{k w} \quad (2.21)$$

This shows that the rest lengths of the springs are a function of all configuration parameters.

The system of Figure 2.2c is linearized in configuration (\mathbf{C}) using the partial derivatives, as explained in Section 2.2, equation 2.3. The absolute- and relative linearization error can then be derived using equation 2.6 and 2.8. The symbolic derivation of the errors is too lengthy to be shown without making additional assumptions. However, the linearization error is still a function of all configuration parameters.

2.6. Results

2.6.1. 1D non-linear model results

The (maximum) linearization errors, $Y_1 = |\epsilon_{\text{tot}}|$, $Y_2 = \left| \frac{\epsilon_{\text{tot}}}{F} \right|$, due to disturbance (\mathbf{V}) will be determined for all configurations (\mathbf{C}) for the three models.

Equation 2.14 shows that the configuration height (z_r) has no effect on the absolute linearization error. Only the system parameter (k) and the disturbance (δ) affect this error. This effect is also shown in Figure 2.3a with respect to the magnitude of disturbance, with different values for k . An increase in unloading force (F^*) only affects the relative linearization error, as shown in Figure 2.3b. For its range of perturbation and unloading force, the error values stay below an absolute linearization error of 3 N and a relative linearization error of 4 % for the nominal value of k . This simple model indicates the effect of spring stiffness, unloading force and disturbance for non-linear systems.

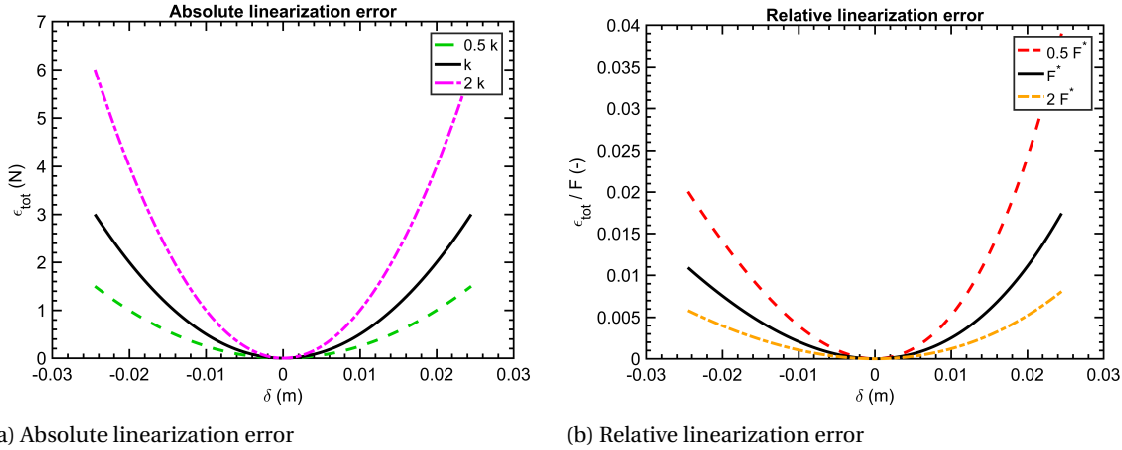


Figure 2.3: Absolute- and relative linearization errors for a 1D non-linear spring model, with respect to the disturbance (δ), stiffness (k) and unloading force (F^*).

2.6.2. 2D non-linear model results

Figure 2.4 shows the maximum linearization errors (Y_i) with respect to the configuration parameters (z_r, F^*) for a fixed spring stiffness k . It is shown that the location of z_r , or configuration height of the subject, has a large influence on the linearization error. Also, it shows that the unloading force has a small influence on the absolute linearization error (Fig. 2.4a) compared to the configuration height z_r , but a large influence on the relative linearization error (Fig. 2.4b). However, for the range of unloading forces and configuration height, the error values stay below a maximum absolute linearization error of 9 N and a maximum relative linearization error of 3 %.

2.6.3. Parallel model results

Figure 2.5 shows the maximum linearization errors (Y_i) with respect to the configuration space (y_r, z_r) as contour plots for a fixed spring stiffness k and nominal unloading force ($F_y^* = 0, F_z^* = 30\%$). The unloading force has a limited influence on the maximum absolute linearization error compared to the configuration location of the endpoint. Therefore, this influence is not shown these figures. It does have an influence on the relative linearization error, as was demonstrated in Figure 2.4b. However, for this model, these linearization errors were still bound to a maximum of 11 N and 3 % for the absolute- and relative error respectively, using

the lowest BWU of 15 %.

The results of Figure 2.5a show that the top corners of the workspace have a higher absolute linearization errors compared to the nominal configuration. The lower regions of the workspace tend to have lower linearization errors. This is expected because the stiffness in y-direction decreases and more pendulum-like behaviour is approached. The relative linearization error, shown in Figure 2.5b, has a similar patterns as the absolute error. For this range of perturbations, rest configuration and unloading force, the error values stay below an absolute linearization error of 11 N and a relative linearization error of 3 %. These maximum error bounds can be taken into account when adding the different error sources for the tracking error (Fig. 2.1).

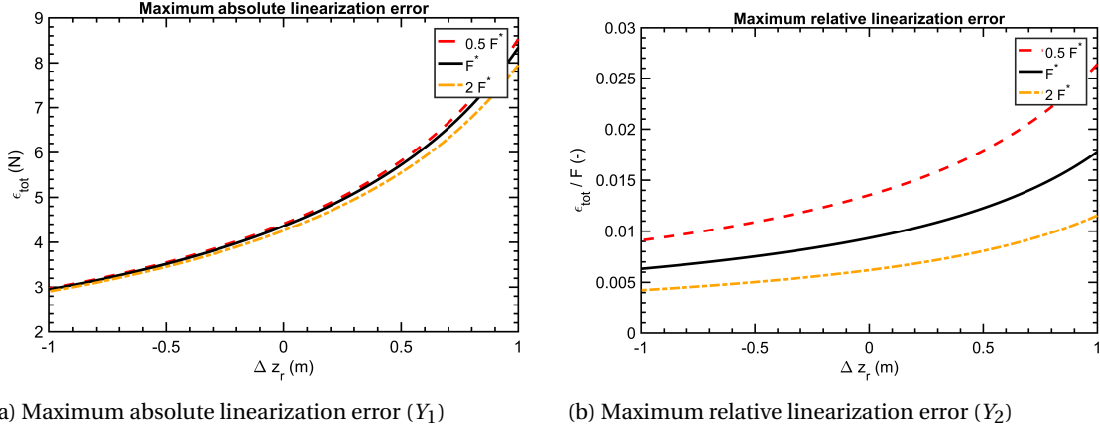


Figure 2.4: Maximum absolute- and relative linearization errors (Y_i) for a 2D linear spring model, with respect to the configuration (z_r, F^*).

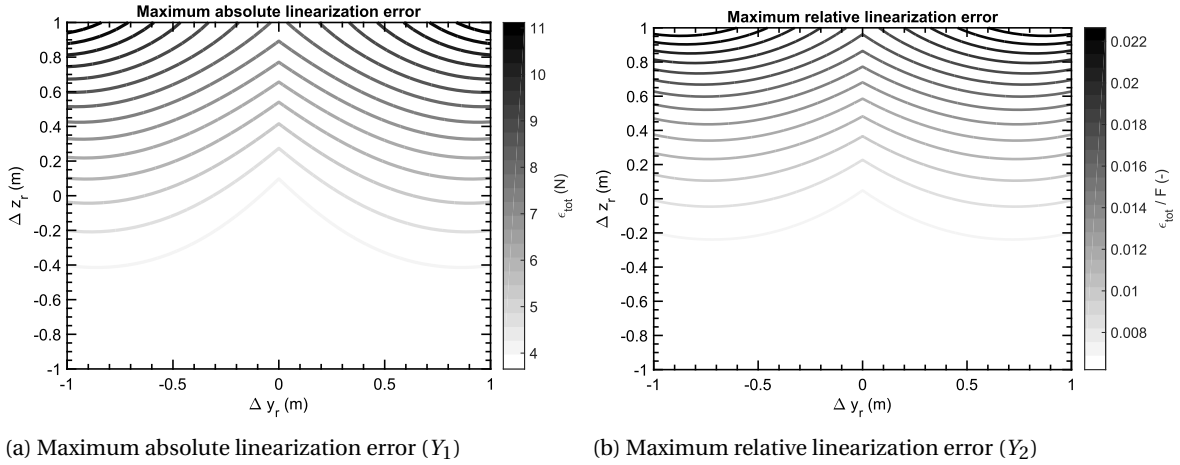


Figure 2.5: Maximum absolute- and relative linearization errors (Y_i) for a parallel spring model, representing the RYSEN, with respect to the configuration (y_r, z_r). The unloading force (F^*) is depicted only for the nominal linearization errors, as there is little influence on the absolute linearization error and only puts a scalar on the relative linearization error.

2.7. Discussion

2.7.1. Threshold of non-linearity

This chapter describes the non-linearity of models with respect to the configurations and perturbations. The thresholds for maximum errors could be determined based on the application of the device that needs to be evaluated. Also, certain directions or linearization errors can be more important than others, depending on the influence to human walking. This work does not address acceptance of these maximum linearization errors.

However, the metrics introduced in this chapter are conservative measures to give an uncertainty range of non-linearity. The error boundaries are determined to be ≤ 11 N and 3 %, for the absolute and relative linearization error. The actual experiments, using a one-dimensional test setup, will determine the performance with this uncertainty range in mind.

2.7.2. The influence of force modulation on linearity

The linearization errors were determined for static models. In reality, the position of the endpoint of the RYSEN will be tracked by decoupled actuators [7]. This will lower the linearization errors as the relative disturbance (V) will be lower and the forces remain closer to the desired values. The quality of sensing, control and actuators will therefore not only influence the force tracking error, but also the linearization error. This notion is especially important for larger perturbations, such as walking in the forward direction, which is not discussed in this chapter.

2.8. Conclusion

Disturbing a BWS system in one direction at a time seems reasonable for the systematic performance evaluation of the RYSEN. This conclusion is supported by calculations for the linearization errors with respect to the perturbation size and configuration, determined for static spring systems, representing BWS systems. These errors stay within threshold 11 N and 3 % for the simplified RYSEN model. In addition, discussions are presented for threshold of non-linearity and influence of force modulation.

3

Methods II - Configuration selection for RYSEN evaluation

3.1. Overview

Many different combinations of configurations can be subject to performance evaluation: the three-dimensional workspace location and body weight unloading (BWU) force. Sensitivity analysis can help to limit the number of configurations by determining the configuration parameters that influence system characteristics the most. This chapter gives an introduction to sensitivity analysis (SA) and determines Sobol's indices based on a simplified static parallel spring model of the RYSEN, which was introduced in Chapter 2. This is used to qualitatively decide on a sampling strategy.

First the metrics for the sensitivity analysis are derived. These metrics are based on a weighted stiffness matrix, as the stiffness matrix is directly related to the system characteristics subjected to a set of perturbations. Then the changes in the stiffness matrix with respect to the nominal configuration will be determined, using variance-based sensitivity analysis. This will indicate if a certain configuration parameter needs to be sampled most thoroughly. Finally, recommendations are made for the minimally required test configurations.

3.2. Selected metrics and weight factors

3.2.1. Metrics

The parallel spring model representing the RYSEN is evaluated, which was introduced in Section 2.5.4. The transparency or tracking error ($\epsilon_{t,i}$) is defined as the difference between configuration force (F_i^*) and the actual force (F_i) under disturbance V and configuration C :

$$\epsilon_{t,i} = F_i - F_i^* = f(C, V) \quad (3.1)$$

For static systems with small disturbances, F_i is directly related to the stiffness matrix (\mathbf{k}), as the size of disturbance and stiffness matrix determines the deviation from F_i^* .

$$\begin{bmatrix} F_y \\ F_z \end{bmatrix} = \mathbf{k}\mathbf{X} \quad (3.2)$$

with

$$\mathbf{X} = \begin{bmatrix} y \\ z \end{bmatrix}, \quad \mathbf{k} = \begin{bmatrix} k_{y,y} & k_{y,z} \\ k_{z,y} & k_{z,z} \end{bmatrix}$$

The elements of the stiffness matrix are determined using the partial derivatives in configuration C :

$$k_{i,j} = \frac{\partial F_i}{\partial X_j} = f(C) \quad (3.3)$$

3.2.2. Stiffness ellipsoids

Stiffness ellipsoids can visualize the stiffness matrix with respect to the configuration. The axes of the ellipsoid represent the direction and magnitude of the eigenvectors and eigenvalues respectively. This approach is used for example by Verhoeven [12] for cable-driven parallel mechanisms. Figure 3.1 shows the stiffness ellipsoids of the simplified RYSEN model (Chapter 2), with respect to the workspace location.

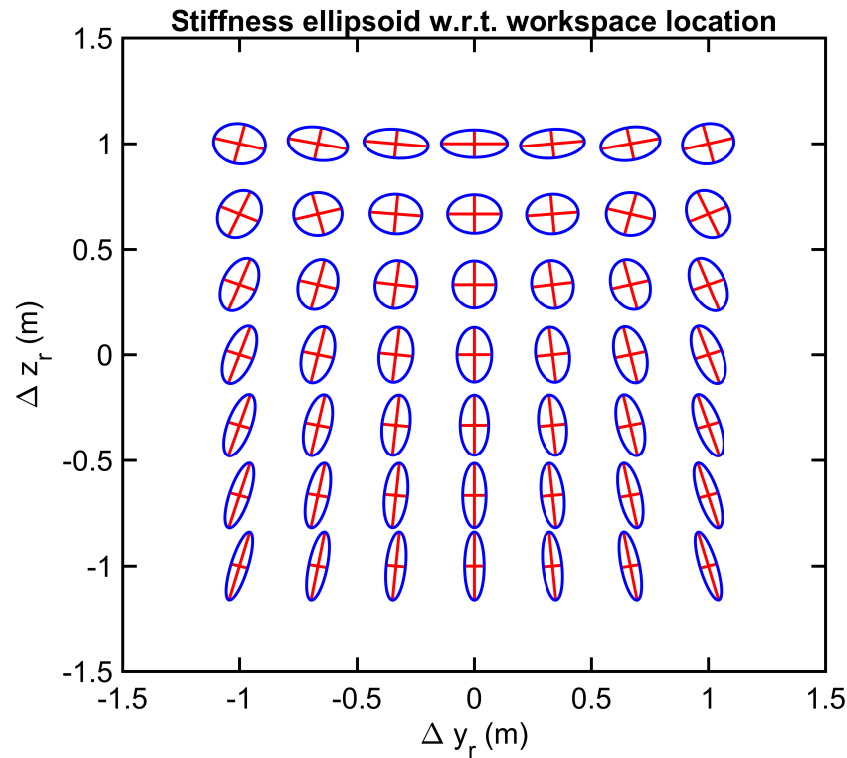


Figure 3.1: Stiffness ellipsoid over the workspace of the simplified RYSEN model from the nominal location in the centre ($x_r = 1.5\text{m}$, $y_r = -2\text{m}$). This gives a visual representation of the eigen-values and -vectors of the stiffness matrix. It shows a strong relation between the location and the shape of the stiffness ellipsoid.

This shows that the lower half of the workspace has the highest stiffness in z-direction. For the top half and more specifically, when the cables make an angle (θ_i) of 45° , the stiffness in y-direction becomes dominant. Also, when the y-configuration is moving away from its nominal position (asymmetry in cable configuration), the stiffness ellipsoid tends to change and rotate. This indicates that the workspace location can strongly influence the performance of the static system.

3.2.3. Assessing the elements of the stiffness matrix

Changes in the elements of the stiffness matrix are shown visually in Figure 3.1 for the y- and z-configuration. However, it is also possible to examine these changes using a sensitivity analysis. This allows for an indication of how thoroughly the configuration parameter should be sampled during actual performance evaluation. To use sensitivity analyses, it is convenient to combine the elements of the stiffness matrix to a single metric. There are multiple options to combine the elements of the stiffness matrix to a single metric, such as using eigenvalues, condition number, average, sum and weight factors for the respective stiffness matrix elements.

All elements of the stiffness matrix contribute to the changes in the force for a set of disturbances. However, not all forces are equally important when considering human walking. The disturbing moment around the base of support (BoS) can be taken as a criteria for the relative importance of disturbing forces. This indicates that using a weighted sum of the stiffness matrix elements could be a good choice to assess the change in stiffness matrix with respect to the configuration.

The entries of the stiffness matrix can be weighted such that they reflect the influence of disturbing moments around the base of support of human walking. Therefore, the human is modelled as an inverted pendulum

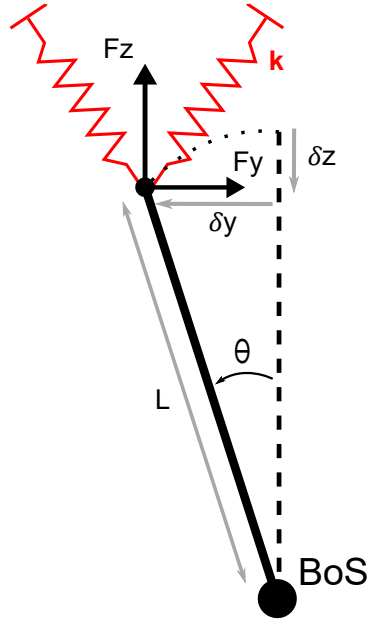


Figure 3.2: Inverted pendulum model to represent the subject connected to the stiffness matrix of the RYSEN model, shown in the frontal plane. This will determine weight factors for the sum of the stiffness matrix.

with zero mass and length L . The model is shown in Figure 3.2 in the frontal plane. It shows the base of support, CoM movement (δ_i) and resulting forces from the RYSEN. Zero mass is chosen as a simplification because the spring forces that disturb walking are important and not the influence of body weight. Also, the base of support is assumed to be fixed as the movements of the CoM are also derived from a fixed position [16].

The forces can be rewritten from Equation 3.2 as:

$$\begin{bmatrix} F_y \\ F_z \end{bmatrix} = \begin{bmatrix} k_{y,y}\delta_y + k_{y,z}\delta_z \\ k_{z,y}\delta_y + k_{z,z}\delta_z + F^* \end{bmatrix}$$

Then, the disturbing moments around the base are calculated using the moment arms as a result of δ_i :

$$\begin{bmatrix} M_{0,y} \\ M_{0,z} \end{bmatrix} = \begin{bmatrix} \cos(\theta)(L - \delta_z)(k_{y,y}\delta_y + k_{y,z}\delta_z) \\ \sin(\theta)(L - \delta_z)(k_{z,y}\delta_y + k_{z,z}\delta_z + F^*) \end{bmatrix} \quad (3.4)$$

where the angle is determined by length L and disturbance δ_i :

$$\theta = \tan^{-1}\left(\frac{\delta_y}{L - \delta_z}\right)$$

This is rewritten in terms of weight factor W_i :

$$\begin{bmatrix} M_{0,y} \\ M_{0,z} \end{bmatrix} = \begin{bmatrix} W_1 k_{y,y} + W_2 k_{y,z} \\ W_3 k_{z,y} + W_4 k_{z,z} + W_5 F^* \end{bmatrix}$$

where the weight factors are a function of the disturbance and geometry.

$$\begin{aligned} W_1 &= \cos(\theta)(L - \delta_z)\delta_y, & W_2 &= \cos(\theta)(L - \delta_z)\delta_z \\ W_3 &= \sin(\theta)(L - \delta_z)\delta_y, & W_4 &= \sin(\theta)(L - \delta_z)\delta_z \\ & & W_5 &= \sin(\theta)(L - \delta_z) \end{aligned}$$

The disturbances δ_i are based on the motion of the center of mass (CoM) during walking [15, 16]. The unloading force (F^*) is selected at 30% BWU for a mass of 75 kg, based on common unloading forces [20]. The

weight factors are normalized to W_{\max} , which in this case is W_1 . The introduction of weight factors makes the stiffness matrix less useful to be interpreted numerically, but more useful for the sensitivity analysis. Length $L = 1$ m is based on the distance from the ground to the CoM from anthropomorphic data of the DINED database [21]. This value is selected as the force application point of the simplified human model.

An alternative is to assign weight factors based only on the size of perturbation. This means that if:

$$\begin{aligned}\delta_z &< \delta_y \\ W_1 &= W_3 = 1 \\ W_2 &= W_4 = \frac{\delta_z}{\delta_y}\end{aligned}$$

Regardless of the choice of W_i , the output function Y will be used for the sensitivity analysis that determines the influence of configuration on the sum of the stiffness matrix elements:

$$Y = f(\mathbf{C}) = (W_1|k_{y,y}| + W_2|k_{y,z}| + W_3|k_{z,y}| + W_4|k_{z,z}|) - \sum |\mathbf{k}_{\text{nom}}| \quad (3.5)$$

where the term between brackets represents the absolute sum of the weighted stiffness matrix in an arbitrary configuration and $\sum |\mathbf{k}_{\text{nom}}|$ is the weighted stiffness matrix in the nominal position, with $y_r = \frac{w}{2} = 1.5$ m, $z_r = -2$ m and $F^* = 0.30 \cdot 75 \cdot 9.81 \approx 220$ N.

3.3. Sensitivity analysis

Sensitivity analysis studies show that uncertainty in the output of a model can be apportioned to input uncertainty for each parameter [22], hence finding the most interesting input parameters. SA is a widely used method, for example for factor prioritization and model emulator design [23]. The methods are generally categorized into local and global SA.

3.3.1. Local sensitivity analysis

Local sensitivity analysis (LSA) determines the influence of small input perturbations on the output with respect to a selected set of input parameters. This is commonly done using the partial derivatives of the output function.

$$LS_p = \left. \frac{\partial Y}{\partial C_p} \right|_{\mathbf{C}_0} \quad (3.6)$$

Equation 3.6 shows the local sensitivity (LS) for output function Y , with respect to configuration C_p , for input parameter p , with \mathbf{C}_0 being the selected initial configuration. This sensitivity can be interpreted such that a relative difference Δ of input parameter p , creates a relative difference $LS_p \cdot \Delta$ on output Y from the nominal configuration.

Figure 3.3 shows the change in the sum of the weighted stiffness matrix (Y) by changing one configuration parameter at a time, while keeping the other parameters in the nominal configuration. The LS_p can be interpreted as the gradient of the slopes from the nominal position. This allows for an easy interpretation in that the weighted stiffness matrix is more sensitive to changes in z_r and that F^* has a very small influence on changes in the stiffness matrix compared to the other parameters. However, this gradient is not constant over the entire range and requires further definition.

The advantage of using LSA is its ease of use. Also, the results give a directional and quantified influence of input parameters. However, LSA has quite some disadvantages. Firstly, the method assumes linearity at its nominal point, as the sensitivity is based on the gradient of its input parameters. This means that for non-linear systems the local sensitivity should be sampled at different points, making it more difficult to interpret. Also, LSA does not allow determination of interaction between input parameters. Because of these shortcomings, a more common approach is to consider global sensitivity analysis of multi-input systems.

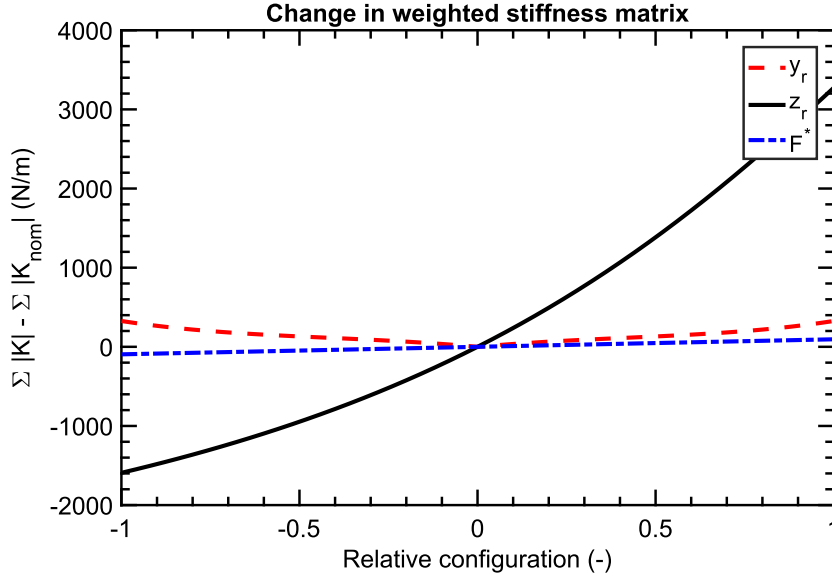


Figure 3.3: Changes in the sum of the weighted stiffness matrix, while changing one configuration parameter at a time. The gradient of the slopes gives a measure for the local sensitivity.

3.3.2. Global sensitivity analysis

Global sensitivity analysis (GSA) takes the uncertainty range of input parameters and determines how it affects variance on the output of the system [23]. In general, the sensitivity is integrated over the input parameter space, often numerically.

Several methods are commonly used for global sensitivity analysis, particularly screening, elementary effect size (EET), variance-based sensitivity analysis (VBSA) and Fourier amplitude sensitivity test (FAST) [23]. In this chapter, VBSA is used to determine the global sensitivity indices, as this method is considered robust [22].

3.3.3. Variance-based sensitivity analysis

VBSA allows identification of which system configurations have the largest influence on the stiffness matrix. VBSA determines the sensitivity indices for single and coupled parameters:

- First-order indices S_p measure the effect of varying C_p alone, but averaged over variations in other input parameters [24]. This metric ranges between 0 and 1.
- Higher-order indices $S_{pq\dots}$ measure only the coupled variances due to the interaction of the input parameters [25]. For example S_{12} is the uncertainty not described by S_1 and S_2 . This metric ranges between 0 and 1.
- Total-effect indices $S_{T,p}$ measures the contribution to the output variance of C_p , including all variance caused by its interactions, of any order, with any other input variables [26]. This metric can be greater than 1.

In this chapter, input p represents the configuration parameters (C). The sensitivity indices can be interpreted in terms of expected reduction in variance if input p is fixed compared to the case for which all inputs are varied simultaneously. This also means that VBSA can give a single estimate of sensitivity while examining the entire input space. A more thorough explanation of the indices can be found in Appendix A.

Numerical toolboxes are often used to determine the sensitivity. Here, the results of two different toolboxes [27, 28] were used and the results found to be similar. These results were also verified with a self-coded script for the 1D non-linear spring system of Chapter 2. These toolboxes allow for multi-input, multi-output systems and use numerical estimators (see Appendix A) to determine the indices [24, 26]. The toolboxes rely

on (quasi-)Monte Carlo, or (quasi-)random, sampling within the configuration space. The Fourier Amplitude Sensitivity Test (FAST) can be implemented with the same toolboxes, allowing for a confirmation of the results of the first-order indices.

3.3.4. VBSA sampling approach

The sampling ranges are chosen as described in Chapter 2, Table 2.1. The toolbox of Cannavo [27] was found to be most efficient for this application.

The number of samples was selected to be 10,000 and the sensitivity analysis was run for 5 times, based on the recommendations of looss and Lemaître [23]. This resulted in a low standard deviation for the resulting sensitivity indices ($< 10^{-3}$ (-)). For this system, the trade-off between accuracy and computation time is not that important as a simplified model is used. Monte Carlo sampling of quasi-random Sobol variables was used. This tends to improve efficiency in covering the configuration space [22].

3.4. Results

Table 3.1 shows results of the first-order (S_p) and total-effect indices ($S_{T,p}$) on the stiffness matrix for different types of weight-factors for configuration p .

Table 3.1: Sobol's sensitivity indices on the weighted stiffness matrix, over the entire range of configurations. Three different weight-factors are used: none, disturbance-based and disturbing-moment-based, the latter given in bold

	S_{y_r}	S_{T,y_r}	S_{z_r}	S_{T,z_r}	S_{Fz^*}	S_{T,Fz^*}
<i>Total sum</i>	0.6943	0.9902	0.0044	0.3005	0.0050	0.0058
<i>Weighted sum (δ_i)</i>	0.4024	0.5780	0.4182	0.5938	0.0034	0.0041
<i>Weighted sum (M_0)</i>	0.0426	0.0708	0.9268	0.9551	0.0022	0.0024

It is also possible to only take the top range or bottom range for the z-configuration. Table 3.2 shows range-dependent results for the weight-factors based on M_0 .

Table 3.2: Sobol's sensitivity indices on the weighted stiffness matrix, over different ranges of the z-location, for the M_0 weight-factor (disturbing-moment-based).

	S_{y_r}	S_{T,y_r}	S_{z_r}	S_{T,z_r}	S_{Fz^*}	S_{T,Fz^*}
<i>'Top' range</i>	0.0409	0.0863	0.9037	0.9489	0.0099	0.0104
<i>'Bottom' range</i>	0.2020	0.2147	0.7692	0.7819	0.0160	0.0162
<i>Complete range</i>	0.0426	0.0708	0.9268	0.9551	0.0022	0.0024

The results show that both the selected weight factors and the location-range has a large influence on the sensitivity of the configuration parameters. When assuming a weighted sum based on M_0 and the complete range of configuration, it is clear that z_r has the largest influence on changes in the stiffness matrix. The total effect index indicates coupling between x_r and z_r . This means that grid sampling throughout the workspace might be necessary for thorough performance evaluation. Moreover, it is seen that the unloading force (F^*) has a very low sensitivity to changes in the stiffness matrix. This means that the influence of unloading force can be tested at one location of the workspace and not at all locations. However, it is still important to determine the effect of F^* on $\epsilon_{t,i}$, but the effect is expected to be the same in every position for this static model.

This approach of sensitivity analysis gives an indication of the most important configuration parameters that should be sampled such that the performance of the system can be adequately evaluated. This approach is discussed in the next section.

3.5. Discussion

3.5.1. Level of complexity

It is assessed that the combination of stiffness ellipsoids, LSA and GSA gives a clear indication of the sensitivity in the configuration space. Inevitably, this represents a trade-off of complexity:

Multiple metrics are difficult to interpret and compare. This is why the multidimensional model was transformed into a single metric: the sum of a weighted stiffness matrix. In return, converting the problem into a single metric, combined with GSA, gives a 'black box' approach. However, the approach has been deemed useful for the goal of selecting the most important configurations.

3.5.2. From VBSA results to experiments

With the measure of sensitivity, it is possible to determine the relative amount of sampling points that are required for a configuration parameter. This is still merely an indication on how much to sample, not where to sample. Two more challenges arise when planning for experimental evaluation, regardless of the stiffness matrix: the chosen grid and the available time.

VBSA does not show 'how' the performance changes. For example, Figure 3.1 shows that the y-configuration has a predictable way of 'rotating' the stiffness ellipsoid. Therefore, it may not be needed to test the configuration space as a grid, based on relative sensitivity, to show this influence. The provided method does not give a recommendation on where to sample, other than a distributed grid. Finally, the actual performance experiments will be subjected to the available time with the RYSEN. Future work will determine which configurations are most interesting to test thoroughly. It might be sufficient to show that the device performs adequately on the bounds of the configuration space.

3.5.3. Model simplification

Actuation, sensing, control, backlash, friction and other characteristics are present in the RYSEN, but not in this static model. Particularly, it is expected that the quality of sensing and actuation will have a large effect on the force tracking error, but little effect on the stiffness matrix.

The use of a complete dynamic model can confirm how the configuration changes the performance of the system. This could be done with the dynamic model of the RYSEN, created by Motek. However, 10,000+ model evaluations for a single sensitivity index would have been an inefficient way to determine the influence of configuration on the performance, as the computation time of each iteration is around 20 to 30 s. For complex, higher dimensional models, it is suggested to start with a simplified model and use that information for more complex emulators. For example, the presented static models could be expanded with first-order models representing the actuators with limitations in speed and acceleration.

3.5.4. Connection to harness

The presented model considers the stiffness matrix at the central point of suspension (CPS) of the RYSEN. In reality, the subject is connected to the RYSEN through a harness. A simplified dynamic model of this connection is introduced in Figure 3.4. The transfer function between the perturbation and motion of the CPS helps to understand the influence of unloading force and lateral stiffness on the motion. It is expected that these dynamics will influence the performance of the system.

The equations of motion are as follows:

$$m\ddot{y} + ky = F^* \sin(\theta) \approx F^* \left(\frac{y' - y}{L} \right) \quad (3.7)$$

which gives the Laplace transfer function between the motion of the disturbance and endpoint:

$$H(s) = \frac{Y(s)}{Y'(s)} = \frac{F^*}{mLs^2 + kL + F^*} \quad (3.8)$$

with CPS mass $m = 2$ kg, disturbing motion y' , CPS motion y , angle of harness θ , strap length $L = 0.40$ m, lateral stiffness k and unloading force F^* . The accompanying bode plots are shown in Figure 3.5. Figure 3.5a shows that for higher initial unloading forces the static gain increases and the bandwidth is higher. In Figure 3.5b, the higher lateral stiffness shows a lower static gain. This means that both the unloading force and the lateral stiffness have an influence on the transfer function. This concludes that, although the unloading force has little influence on the stiffness matrix, the effects of unloading force have to be shown in at least one location of the workspace.

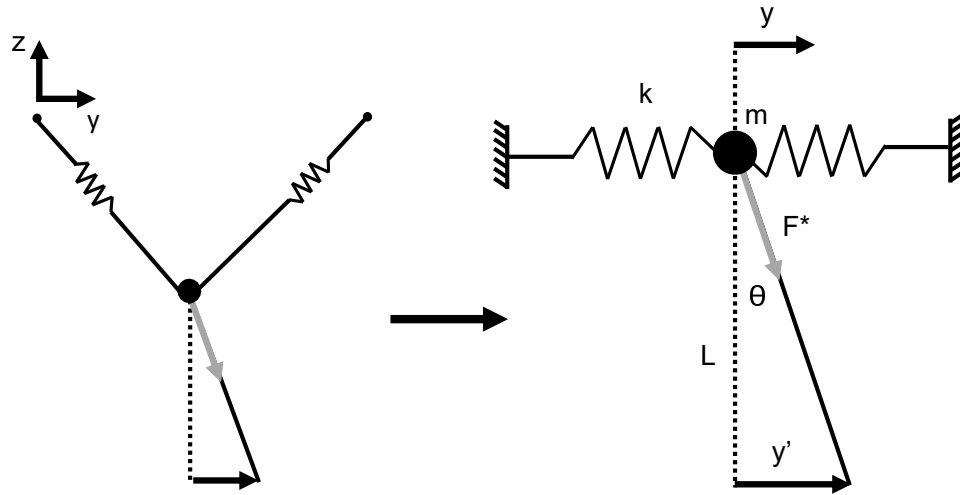
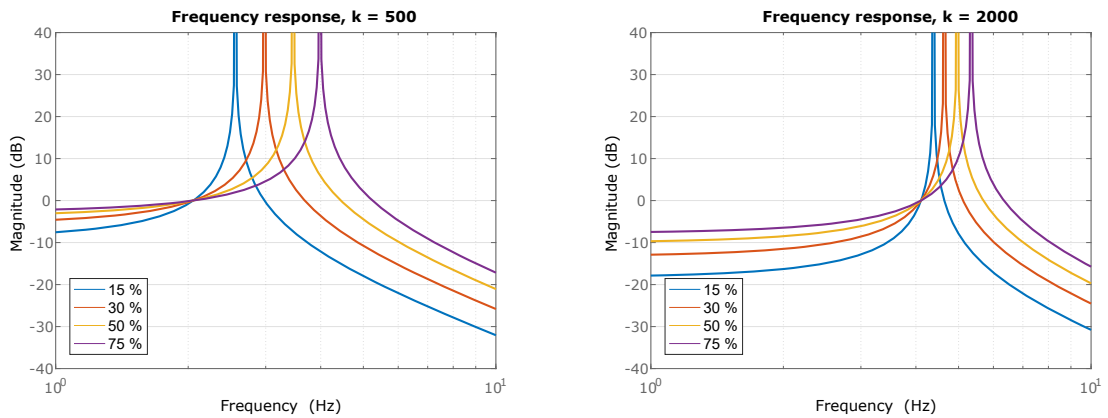


Figure 3.4: RYSEN model simplification to determine the influence of strap length, stiffness and unloading force on the dynamics in the lateral directions. The lateral stiffness is based on Section 3.2.2. The strap length ($L = 0.5\text{m}$) is chosen to be constant.



(a) $k = 500 \text{ N m}^{-1}$

(b) $k = 2000 \text{ N m}^{-1}$

Figure 3.5: Bode plots for the simplified lateral perturbation model, representing the connection between the RYSEN and the subject through a harness. This can show the influence of unloading force (F^*), stiffness (k) and strap length (not depicted).

3.6. Conclusion

Sensitivity indices show how large the influence of configuration is to the change of the weighted stiffness matrix. The vertical location in the workspace tends to have the highest influence to change, whereas the unloading force has negligible effect on the stiffness matrix. However, the unloading force does have an influence on the strap connection to a subject. These notions help to indicate the configuration parameters that need to be tested most thoroughly.

4

Methods III - Experimental evaluation of body weight support systems

4.1. Overview

This chapter introduces a systematic performance evaluation for the RYSEN and other active body weight support systems. First, the experiments and performance metrics of BWS systems are listed, based on earlier work [10]. Secondly, the configuration parameters are chosen based on the results of Chapter 3. Then, the experimental protocol is discussed along with methods of limiting the number of tests. These findings are summarized as the selected experiments. Finally, a test setup is introduced that can give sinusoidal perturbations to the endpoint of the BWS systems for the range of magnitudes and frequencies, simulating the perturbations a subject can give during walking.

4.2. Experiments, metrics and configurations

4.2.1. Experiments

Three experiments can evaluate the force tracking performance of active BWS systems [10]. Similar experiments are suggested in the study of Parietti et al. [29] for a haptic interface.

1. Static force tracking
2. Force output tracking
3. Disturbance rejection or 'zero-impedance mode'

The 'static force' experiment determines the difference between the force at the endpoint and the constant desired force. This can be measured before starting the other two experiments.

The 'force output' experiment consists of determining the bandwidth of the output force of the device. In this case, the endpoint of the test setup is fixed and a force signal is commanded with a selected frequency and magnitude. It is important that the product of the frequency and amplitude of the signal remains constant to create a frequency response.

For the 'disturbance rejection' experiment, a constant unloading force is tracked while a position disturbance is given to the device at the endpoint. These perturbations are within a range of amplitudes and frequencies related to human walking.

4.2.2. Metrics

The performance metrics will give a measure of transparency, or how well the required forces can be tracked. This is determined as the estimation error and the tracking error; for the static force tracking, force output and disturbance rejection case:

- Estimation error (ϵ_{est}) - N
 - Peak and root mean square (RMS) errors
- Tracking error (ϵ_t) - N
 - Peak and RMS errors
- Force and disturbance rejection bandwidth - Hz
 - Useful frequency range
 - Half-power bandwidth

Estimation error: This is the difference the force estimation of the RYSEN and the actual measured forces. It is useful to have a measure of force estimation error with an external sensor, because the RYSEN force sensors are non-collocated with the CPS.

Tracking error: This is the difference between the desired force and measured force, either by the RYSEN or the external test setup. This is the a common performance metric to measure transparency.

The standard deviation can be determined when multiple cycles are performed in a single configuration. This gives a measure of variability. The bandwidth will give the range of frequencies for which the device can still produce or track the required forces. The limits are often depicted as the half-power (-3 dB) bandwidth. However, it is also possible to determine the useful frequency range: the range of frequencies where the gain stays constant.

The goal is to check these metrics over the range of configurations, frequencies and disturbances relevant for the device and human walking.

4.2.3. Configurations

An overview of the configurations of the experiments can be found in Table 4.1. This shows that the number of configurations are reduced based on the results of Chapters 2 and 3.

Table 4.1: Overview of the configurations of the performed experiments. The bold values indicate the nominal configuration.

Configuration	Symbol	Values	Metric	Based on
Body weight unloading	BWU	[30 , 15]	% weight of subject	Common BWU force [20]
Bias force	B	[0 , 3]	% weight of subject	Novel assistive force [4]
y-location	y_r	[0 , 1]	relative from centre	Normalized location [17]
z-location	z_r	[0 , -1]	relative from centre	Normalized location [17]
Strap length	-	[0.40 , 0.60]	m	Regular strap length

First of all, the directions of disturbances are separated, based on the results in Chapter 2. The principle of superposition is assumed, which indicates that there is no need to disturb the system in two directions at the same time to fully determine the performance. Furthermore, two configurations of BWU are chosen, for which 30% is the nominal case, based on common BWU forces [20]. Note that the available sensor only allows forces up to 300 N. The influence of the x-location is assumed to be negligible, due to the degree of freedom introduced by the trolleys of the RYSEN. Therefore, only the centre of the x-range is chosen. The influence of the y-location is assumed to be symmetrical, as was seen in Chapter 3. Therefore, only one edge location of the workspace is tested. For the z-location, a lower location is tested. A higher location cannot be reached with the available means of the laboratory. Therefore, the case of increased strap lengths was introduced. This case introduces the effect of a higher z-location and increased strap length simultaneously. This case will not allow to make a direct conclusion about the influence of location or strap length on performance, but will give an indication. Having a higher platform for the test setup would allow to test the high location, without increasing the strap length.

4.3. Static force tracking

The static force is set and measured at selected locations, for all the configurations. The results will show how accurate the system can unload in a static case and how this unloading is influenced by the estimation error. This is similar to experiments done in [17]. Static force tracking is done with the same setup as the force output and disturbance rejection tests.

4.4. Force output performance

For this experiment, the endpoint of the test setup is fixed. The output force is commanded by RYSEN for the three directions separately and measured at this endpoint. To determine the force bandwidth, a range of frequencies and accompanying force amplitudes are being commanded.

In order to design the input signals over the range of frequencies, a 'base signal' needs to be determined. In this case the base signal is the frequency times the force amplitude. The maximum force amplitude is based on F^* of 30% BWU for a 75 kg person, to make sure that the straps will not go slack. That force is exerted at the lowest chosen frequency of 0.2 Hz. The highest frequency is 3 Hz, based on the frequency content of normal gait [30, 31]. The signal (amplitude \times frequency) remains constant for different average unloading forces. This means that the lowest BWU of 15% can only be measured from 0.4 Hz in z-direction, to prevent the straps from going slack. For the x- and y-directions, a force amplitude of 10% BWU is exerted for the lowest frequency of 0.2 Hz. This is based on a maximum horizontal force assistance of around 10% BWU that was found useful for rehabilitation purposes with a similar BWS system [4, 19]. A constant bias force of 3% is chosen as a non-zero mean case for the horizontal directions of this experiment. This test is additional to the nominal configuration.

To summarize the signals, the required vertical force is $BWU \cdot 75 \cdot 9.81 \pm [220 - 15]$ N and the lateral forces are $B \pm [74 - 5]$ N from 0.2 to 3 Hz, with BWU and B the unloading- and bias forces respectively. The frequency sweep is performed using a step-wise increase over the range of f , using steps of 0.2 Hz, going from 0.2 Hz to 3 Hz. Every frequency step is measured for at least 12 cycles to determine the standard deviation or variability. For the force performance test, the non-nominal cases are not tested in combination, due to the available time with the system.

4.5. Disturbance rejection performance or 'zero-impedance mode'

For this experiment, a position disturbance is given while tracking a constant unloading force. The disturbances are set from 0.01 to 0.05 m and physically adjusted by changing the location on the crank, as will be explained in Section 4.6. The 'base signal' (amplitude \times frequency) must remain constant over the input disturbance range. The signal is based on human walking at 1 m s^{-1} or 1.5 Hz, with an amplitude of 0.018 m [15, 16]. This means that the range of disturbances are tested from 0.45 to 2.25 Hz in order to keep the product of the signal constant. Each point is measured for 15 cycles to determine the standard deviation or variability. The non-nominal cases are tested for only one magnitude of disturbance ($\delta = 0.025 \text{ m}$).

4.6. Test setup

Figure 4.1 shows a test setup that measures forces and delivers position perturbations. It consists of a reciprocal sliding mechanism, similar to a piston, with an external 6D force-torque sensor (ATI Mini45-SI-145-5) that measures resulting forces on the endpoint. This external sensor is needed to determine the force estimation performance of the RYSEN, as its force sensors are not located near the CPS. The external sensor is calibrated by ATI and confirmed by means of a spring scale. The forces (and torques) are directly measured using an analog interface connected to the RYSEN. The forces and motor position are measured at 1000 Hz. The setup can be configured such that it can disturb the device in all three directions. For the z-direction, a spring assists the motor to deliver the required torque to move the endpoint. The endpoint is connected to the test setup using a rod and straps. This simulates the connection of a subject to the RYSEN with a harness. The test setup uses sand bags as a counterweight to the unloading forces of the RYSEN. The 'piston rod' can be attached to the 'crank' at nine different locations that result in different magnitudes of perturbation. For the oscillation frequency of the perturbation, a (velocity) control module (Beckhoff AX5201) is applied to the motor (Beckhoff AM8022-LP070S-MF1-7). This mechanism results in the following reciprocal motion of the

endpoint:

$$x = r_{\text{cr}} \cos(\theta) + l \cos(\gamma) \quad (4.1)$$

$$\gamma = \sin\left(\frac{r_{\text{cr}} \sin(\theta)}{l}\right)^{-1} \quad (4.2)$$

with x being the endpoint location, r_{cr} the radius of the crank, θ the motor angle and l the rod length to the slider. Using a reciprocal mechanism is an approximation of a perfect sinusoid. When l approaches infinity, a perfect sinusoid of $s = r \cos(\theta) + l$ is achieved. However, Figure 4.2 suggests that the test setup is still a good approximation of a sine-wave for $r = 0.05$ m, $l = 0.3$ m and $f = 2$ Hz for the worst-case scenario of perturbation.

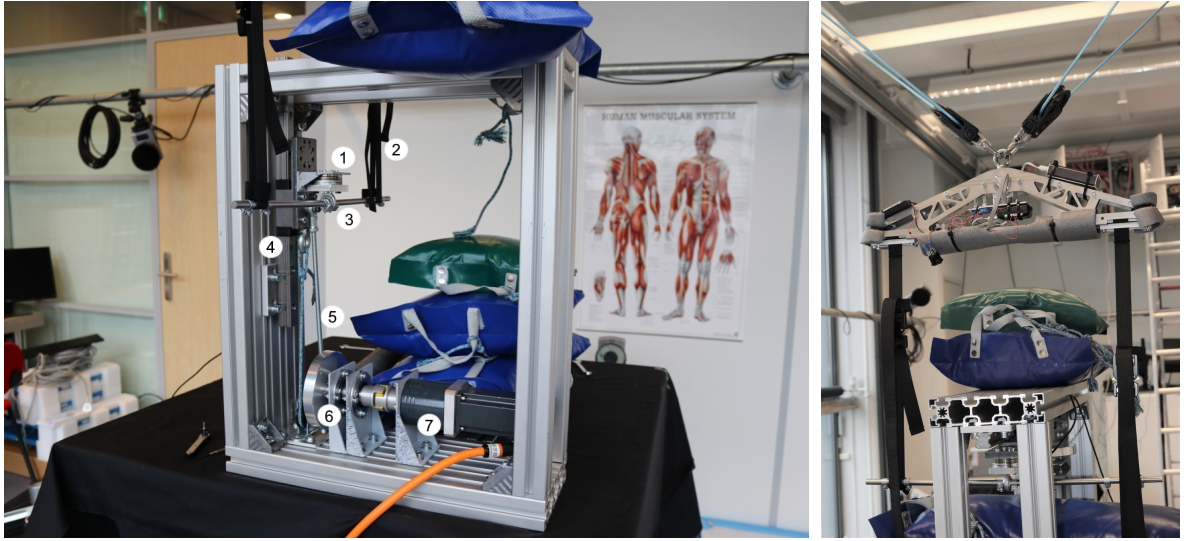


Figure 4.1: Test setup for the systematic performance evaluation of the RYSEN in three directions, shown in the vertical and horizontal configurations. The identifiers represent the endpoint and sensor (1), straps (2), rod and bearing (3), slider and cart (4), piston rod (5), crank (6) and motor (7).

4.7. Data processing

The input and output signals are collected by the RYSEN. The measured forces are filtered using a 4th order low-pass Butterworth filter at 50 Hz. For each measurement point, the first three cycles are removed to allow that steady-state is reached. The RMS and peak errors of the estimation and tracking errors are determined over all cycles of a frequency point. The cycles are isolated to determine the frequency response. Each isolated cycle will be fit to a sine response (time domain) using least squares. The mean and standard deviation of the isolated cycles of a frequency point are used to show the frequency response (gain, phase, offset) and variability. The sine response is fitted as follows:

$$C_0 \sin(ft - \phi) + O = C_1 \sin(ft) - C_2 \cos(ft) + O \quad (4.3)$$

$$C_0 = \sqrt{C_1^2 + C_2^2}$$

$$\phi = \text{atan2}(C_2, C_1)$$

with known frequency point f , time t , the four-quadrant arctangent atan2 and parameters C_i and O . The parameters will give the values of the gain ($C_0 / \max(S_{\text{in}})$), phase (ϕ) and offset (O), where S_{in} represents the input signal. The linearized matrix equation that needs to be solved through least squares is:

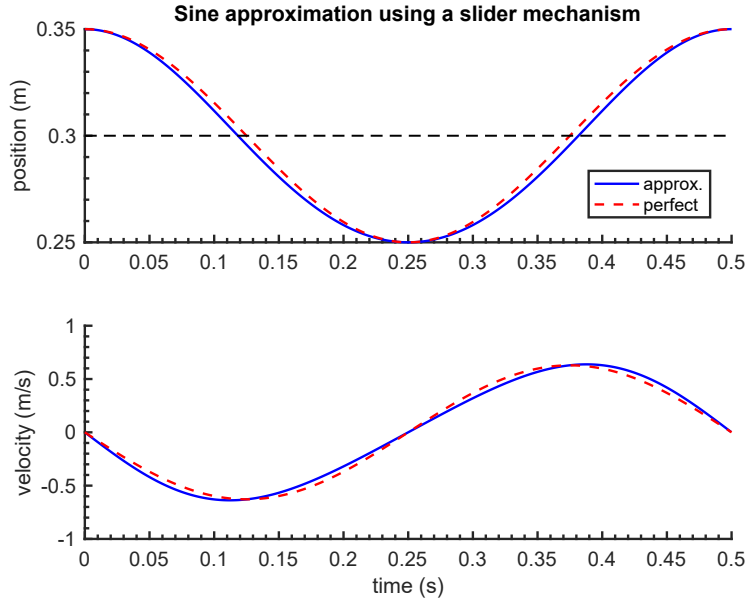


Figure 4.2: Approximation of a sine wave using the reciprocal mechanism of the test setup. The approximation is shown for the worst-case scenario of $\delta = 0.05$ m and $f = 2$ Hz.

$$\mathbf{Ax} = \mathbf{b} \quad (4.4)$$

$$\mathbf{A} = \begin{bmatrix} \sin(ft_1) & -\cos(ft_1) & 1 \\ \vdots & \vdots & \vdots \\ \sin(ft_n) & -\cos(ft_n) & 1 \end{bmatrix}, \quad \mathbf{x} = \begin{bmatrix} C_1 \\ C_2 \\ O \end{bmatrix}$$

with \mathbf{b} the output data that need to be fit to a sine response, solving for parameters C_i and O . The results of the isolated sine responses are visualized using the mean and standard deviation at a frequency point.

4.8. Conclusion

This chapter introduced the experiments, metrics, configuration reduction and input signals for the performance evaluation of 3D active BWS systems. The configuration reduction was based on the qualitative results of Chapter 3 and the available time with the RYSEN. The proposed experiments and input signals were based on human walking and support strategies. Furthermore, a test setup was introduced that can disturb a BWS system in arbitrary direction while measuring the resulting interaction forces. This allows to objectively measure the frequency response, tracking and estimation error. Finally, a protocol was given for data processing to retrieve the desired metrics.

5

Results - Performance of RYSEN

5.1. Overview

This chapter shows the results of the experiments introduced in Chapter 4. First, initial observations are given on the experiments. Then the different types of experiments are examined for the nominal and non-nominal cases. Finally, remarks and improvements on the chosen methods are given in the discussion.

5.2. Initial observations

In the current setup, a disturbance in y-direction induced unstable behaviour. Also, the force estimation errors tended to increase when the frequency increased and instabilities occurred. Furthermore, in some instances drift was observed in both lateral directions, meaning that force control would account for the disturbance, but with a force bias drifting around the desired force.

Two non-nominal cases were not performed: First, the non-nominal disturbance rejection cases in y-direction were not performed due to the observed instabilities. Second, the x-direction, force output experiment for low BWU (15 %) was not performed. This was because when trying to render large lateral forces with a low BWU, a large angle and fast motion was required to create the lateral force, which made the system unstable.

In figure 5.1, two examples of 'raw' data show the sensor/estimated forces in the force output test and sensor/desired forces in the disturbance rejection test.

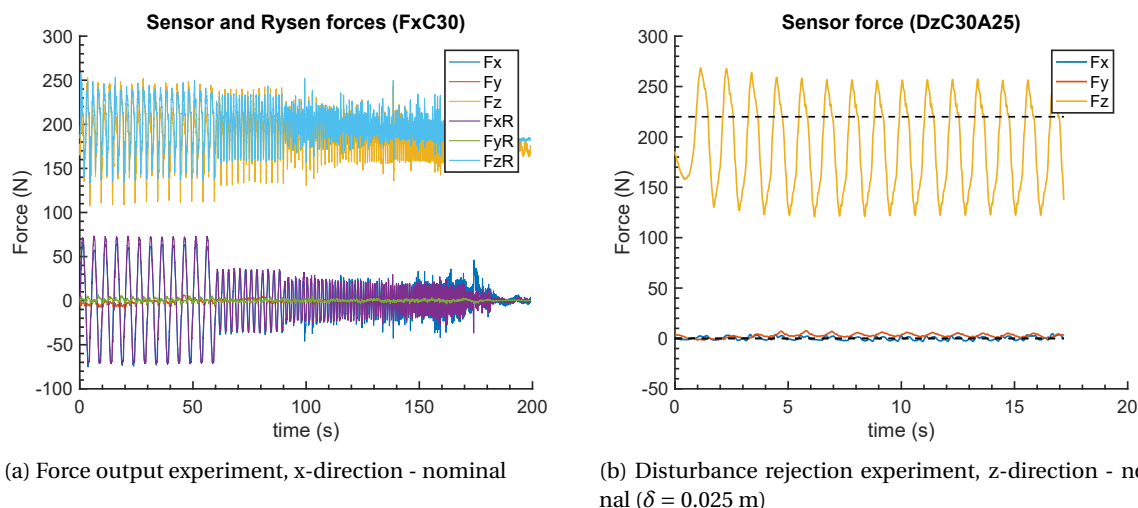


Figure 5.1: Examples of data in time-domain, showing the (a) sensor/estimated forces in the force-output test and (b) sensor/desired forces in the disturbance-rejection test. This data is already filtered using a 4th order, 50 Hz, low-pass Butterworth filter.

5.3. Static force estimate performance

Table 5.1 shows the results for the static tracking error using the measured and estimated forces. It also shows the estimation error, which indicates that part of the tracking error can be explained by this estimation error. The RYSEN has trouble rendering an accurate static force in y- and z-direction. For the y-direction this is almost completely explained by the estimation error. For the z-direction, a known force bias of around 10-30 N is observed when rendering a static force.

Non-nominal cases:

In these sections of the chapter, the anomalies found for the non-nominal cases will be qualitatively presented. The uncertainty in force estimation makes it difficult to make strong conclusions about the influence of configuration on performance. Also, these cases could sometimes only be performed once or twice.

Table 5.2 shows the estimated static error for the non-nominal cases. It shows that a lower BWU tends to give a lower static tracking and estimation errors in z-direction. Also, introducing a bias increases the tracking error in the direction of that force. The higher and edge location did not seem to affect the tracking error or estimation error. Interestingly, the lower location seemed to give a lower estimation error in z-direction (not shown), but its tracking error is still within the range of 30 N.

Table 5.1: Static force tracking results for the nominal location and unloading force, taken over 20 samples. It shows that the tracking error for the lateral directions can be explained by the estimation error, especially in y-direction. The tracking error in z-direction can be explained partly by the estimation error.

Type of static error	$\epsilon_x \pm \text{std}_x$ (N)	$\epsilon_y \pm \text{std}_y$ (N)	$\epsilon_z \pm \text{std}_z$ (N)
Static tracking error - estimated ($F_R - F_{\text{des}}$)	0.70 ± 0.70	1.13 ± 0.82	16.51 ± 11.28
Static tracking error - measured ($F - F_{\text{des}}$)	0.81 ± 0.66	6.77 ± 2.37	30.59 ± 11.78
Static estimation error ($F - F_R$)	0.47 ± 0.34	8.10 ± 1.23	14.66 ± 7.19

Table 5.2: Static force tracking results, using the estimated forces ($F_R - F_{\text{des}}$), for the non-nominal configurations. The number of trials are given between brackets (#). This shows that a lower unloading force gives lower tracking errors. It also shows that a force bias increases the tracking error in that direction. Increased strap length seems to slightly increase the tracking error in y-direction.

Non-nominal cases Static tracking error (#)	$\epsilon_x \pm \text{std}_x$ (N)	$\epsilon_y \pm \text{std}_y$ (N)	$\epsilon_z \pm \text{std}_z$ (N)
Low BWU (5)	0.94 ± 0.92	1.20 ± 0.95	14.46 ± 7.28
Bias force - x (2)	2.64 ± 2.31	0.54 ± 0.48	25.96 ± 19.38
Bias force - y (1)	$0.13 \pm -$	$6.97 \pm -$	$36.96 \pm -$
Edge location (5)	0.56 ± 0.92	0.68 ± 0.71	34.50 ± 9.31
Low location (5)	0.66 ± 0.66	1.08 ± 1.14	32.66 ± 11.37
Straps length (5)	0.26 ± 0.31	2.15 ± 1.25	31.10 ± 14.64

5.4. Output force performance

5.4.1. Notes on the 'dynamic' experiments

In the following sections, the frequency response, tracking error and estimation error are shown for the two 'dynamic' experiments in the three separate directions. For these results, the tracking error is given as $\epsilon_t = F_R - F_{\text{des}}$. This is the tracking error that the RYSEN 'knows' about. In Appendix C, the frequency responses of the non-nominal cases will be presented.

For the frequency response, the dashed lines indicate the gain, phase and offset with the estimated forces of the RYSEN. For the tracking and estimation results, the dashed lines show the cross-talk in the directions that are not disturbed in the experiment.

5.4.2. Output force performance: x-direction

The frequency response (Fig. 5.2a) for the output force experiment in x-direction shows that the estimated and measured response coincide quite well. For the estimated response there is accurate force rendering up

until 0.4 Hz – i.e. the useful frequency range. There is an overshoot in force rendering at 1.6 Hz. The bandwidth is either 0.4 or 2.3 Hz, depending if the useful-frequency-range or half-power bandwidth is specified [32]. For the measured frequency response, the same bandwidth metrics are 0.4 or 2.4 Hz. The offset or unwanted force bias remains around zero up to 1.6 Hz. For higher frequencies, instabilities occur and offsets can go up as high as 10 N for the measured frequency response.

The RMS tracking error (Fig. 5.2b) in x-direction is around 10 N until the oscillation/overshoot occurs. Peak tracking errors in x-direction go up to 30 N during overshoot. Both y-errors remains constant and below 5 N. The peak tracking error in z-direction decreases with the amplitude of the force tracking from 90 to 50 N. The RMS error stays around 30 N over the range of frequencies.

The estimation error (Fig. 5.2c) in x-direction is around 7-20 N for the RMS and peak error respectively. However, for higher frequencies these estimation errors in x-direction go up to 20-50 N. The estimation error in y-direction stays 10 N for both the RMS and peak error. The estimation error in z-direction stays constant and around 20-50 N for the RMS and peak error respectively.

Non-nominal cases:

Figure C.1 shows the non-nominal frequency responses. The lower BWU case was not performed because the RYSEN had to make large and fast movement to render the lateral forces, which made the system unstable. The introduction of a bias force or the edge location does not notably change the performance. Increased strap length causes a slightly larger overshoot, which could be incidental. A lower position has a smaller overshoot. This case also shows smaller tracking and estimation errors (not shown).

5.4.3. Output force performance: y-direction

The frequency response (Fig. 5.3a) for the output force experiment in y-direction shows a large difference between the estimated and measured results. The measured frequency response shows a higher gain and instabilities and does not indicate a useful frequency range. It shows high standard deviations in the gain from 1 Hz onward, indicating oscillatory or unstable behaviour. It also shows unwanted force bias, as can be observed with the offset, up to 15 N. The estimated frequency response shows a useful frequency range up to 0.6 Hz and a half-power bandwidth of 1.3 Hz. The instabilities are also observed for the estimated frequency. The offset however stays around zero, which is not the case for the measured frequency response. This indicates that the bias in force estimation can be responsible for the differences between the frequency plots.

The tracking error (Fig. 5.3b) in y-direction remains constant up till 1.2 Hz, with RMS errors around 10 N and peak errors of 40 N. The tracking error in x-direction remains below 10 N for both the RMS and peak errors. The z-error is similar in magnitude as in the x-direction experiment, up until the point of unstable behaviour.

The estimation error (Fig. 5.3c) in y-direction is high, even up to 1.2 Hz, with RMS errors of 25 N and peak errors of 50 N. The estimation error in x-direction is around 10-15 N for the RMS and peak error respectively. The estimation in z-direction is around 20-40 N for the RMS and peak error respectively.

Non-nominal cases:

Figure C.2 shows the non-nominal frequency responses. A lower BWU seems to have a steady gain, instead of an increasing one. Drift at higher frequencies is still observed. The force estimation error is lower (not shown), but this could be coincidental. The bias force case seems to be similar in performance. Increasing the strap lengths shows a lower overshoot around 1.6 Hz. The edge location looks to have similar performance. Only for the first frequency point, the virtual wall is reached, due to the angle that needed to be made to produce the lateral forces. The lower location seems more unstable. Especially for higher frequencies the standard deviations and offset become large. Also, the estimation errors in y-direction seem to be worsened for the lower position. This could be incidental due to the instabilities.

5.4.4. Output force performance: z-direction

The frequency response (Fig. 5.4a) for the output force experiment in z-direction shows that for the estimated response, the useful frequency range is 0.4 Hz and the half-power bandwidth is around 1.2 Hz. However, for the measured response the half-power bandwidth is lower with 0.7 Hz. The offset between the estimated and

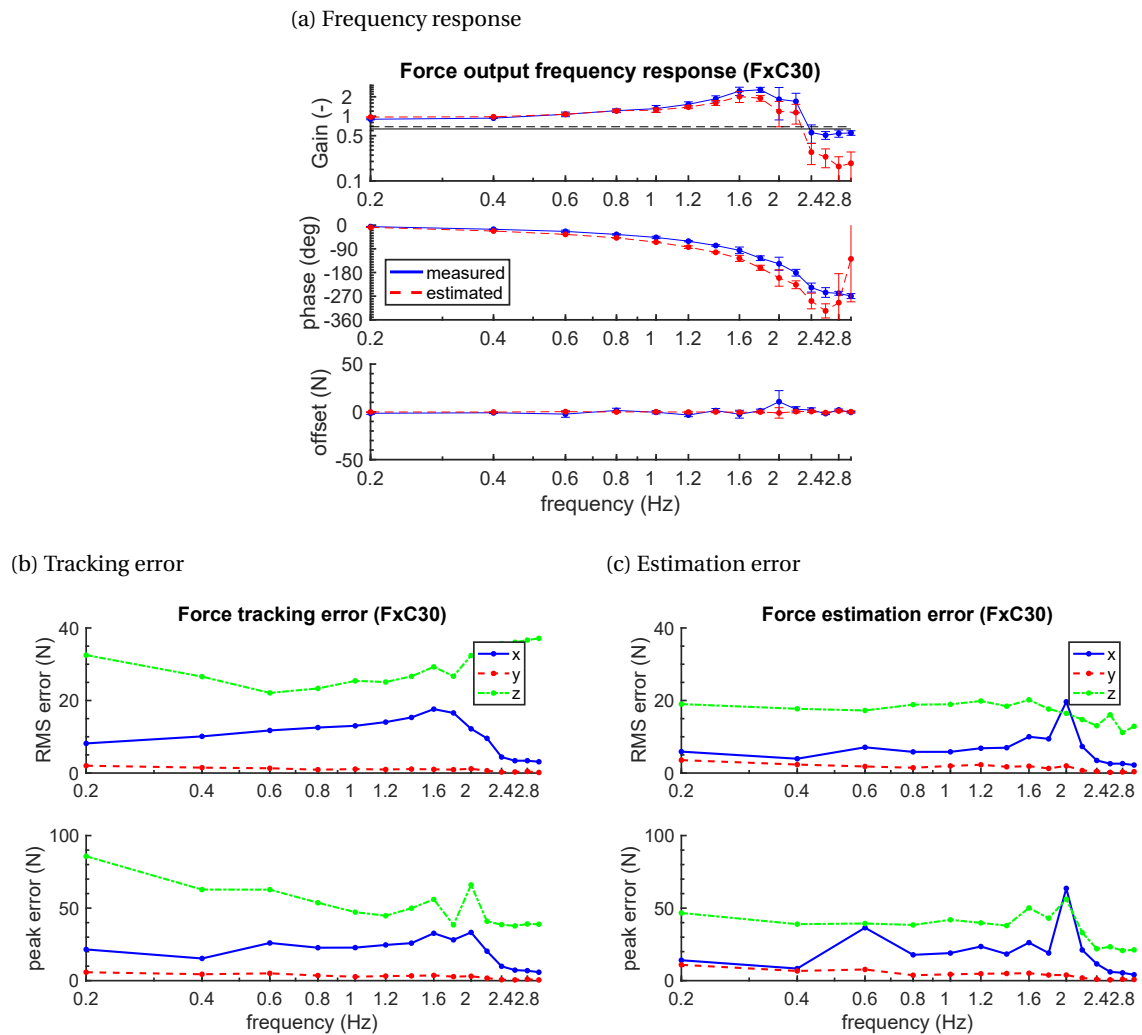


Figure 5.2: Results for the force output experiment, x-direction. (a) shows the frequency response of the measured and estimated forces. The markers indicate the measurement points. The black lines indicate the half-power limit. The offset shows the force offset of the sine-fit. (b)/(c) show the tracking and estimation errors (RMS and peak) in all three directions. The dashed lines indicate the direction not perturbed.

measured frequency response differs up to 20 N. It is expected that this is due to the friction in the system, as 20 N is often observed as the estimation error for the z-direction.

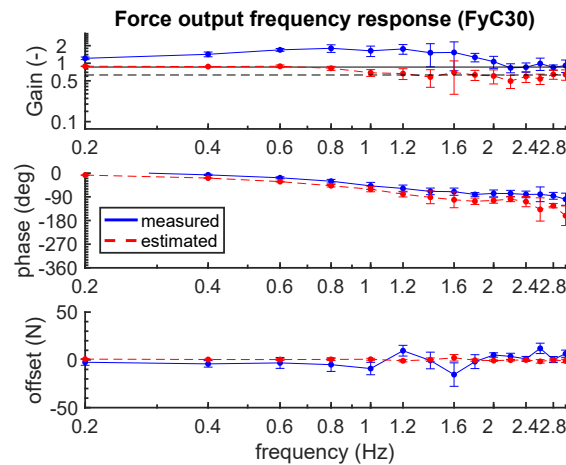
The tracking error (Fig. 5.4b) for the x- and y-direction are below 5 N for the RMS and peak errors. The tracking error in z-direction is 30-50 N for the RMS and peak error respectively.

The estimation error (Fig. 5.4c) for the x-direction is below 2 N. However, for the y-direction the estimation error is high, with 15-20 N for the RMS and peak error respectively. The estimation error in z-direction decreases with the decrease in force amplitude from 25-40 N to 10-12 N for the RMS and peak error respectively.

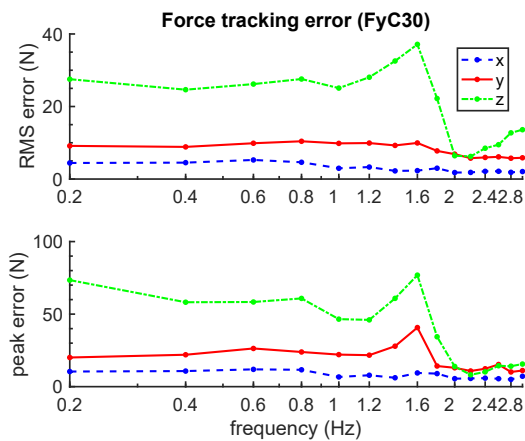
Non-nominal cases:

Figure C.3 shows the non-nominal frequency responses. A lower BWU has a higher bandwidth and steady offset. The estimation errors are also lower (not shown). Increasing the strap lengths seem to give similar performance. However, the estimation error in y-direction is lower, but this could be coincidental. The edge location gives a slightly higher bandwidth. The estimation in y-direction is also better. Both of these findings can be coincidental, as the force estimation errors still dominates performance.

(a) Frequency response



(b) Tracking error



(c) Estimation error

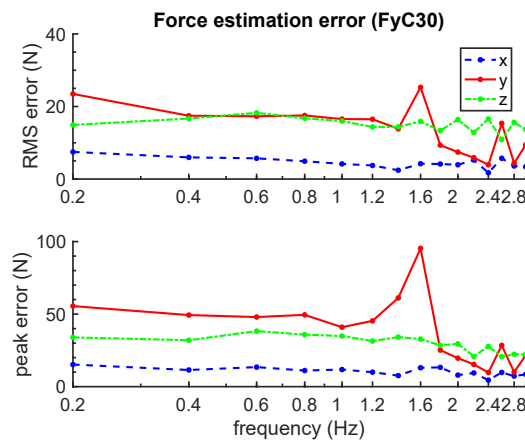


Figure 5.3: Results for the force output experiment, y-direction. (a) shows the frequency response of the measured and estimated forces. The markers indicate the measurement points. The black lines indicate the half-power limit. The offset shows the force offset of the sine-fit. (b)/(c) show the tracking and estimation errors (RMS and peak) in all three directions. The dashed lines indicate the direction not perturbed.

5.5. Disturbance rejection performance

5.5.1. Disturbance rejection performance: x-direction

The frequency response of the disturbance rejection experiment in x-direction (Fig. 5.5a) shows that up to 0.6 Hz the RYSEN controls for the disturbance to a fairly constant gain. Then, after 0.6 Hz, the gain drops due to the decrease of the amplitude and the passive motion in the pulley. The RYSEN does little to control any more for these smaller disturbances. There is a difference between the measured and estimated frequency response, due to a slight overestimation of the forces in x-direction. For the measured frequency response, there is a slight increase in gain for the highest frequency of 2.25 Hz, which could be caused by oscillatory behaviour. The offset of both frequency responses stay below 2 N.

Overall, the tracking- and estimation errors in the disturbance rejection experiments are lower compared to the force output experiment. This is most likely because the motions that are made by the RYSEN are smaller and slower.

The tracking error (Fig. 5.5b) in x- and y-direction remain constant and below 7 N for the RMS and peak errors. The tracking error in z-direction is peculiar, as the results have a saw-tooth shape over the different frequency points. This could be explained by the fact that the experiment was performed in intermittent

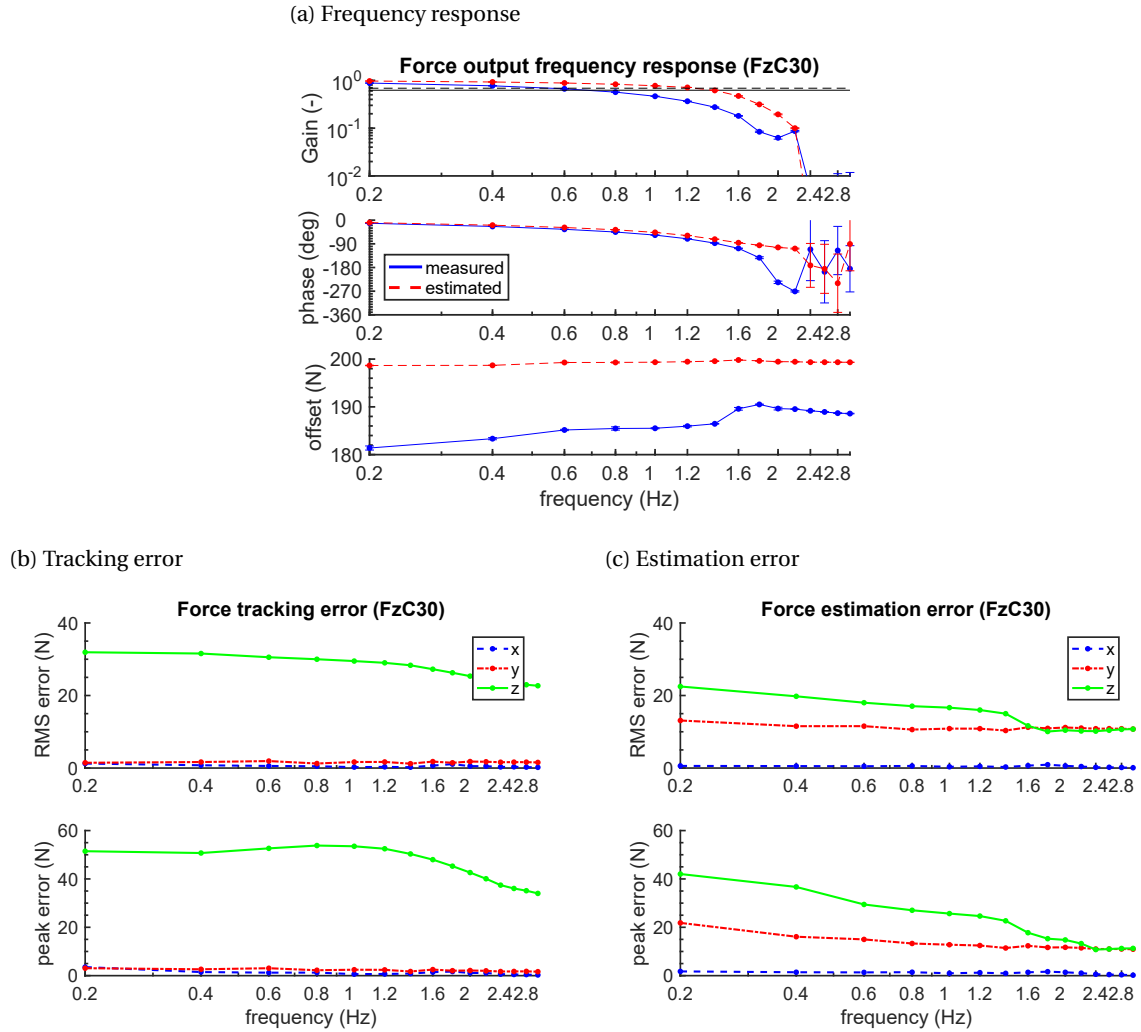


Figure 5.4: Results for the force output experiment, z-direction. (a) shows the frequency response of the measured and estimated forces. The markers indicate the measurement points. The black lines indicate the half-power limit. The offset shows the force offset of the sine-fit. (b)/(c) show the tracking and estimation errors (RMS and peak) in all three directions. The dashed lines indicate the direction not perturbed.

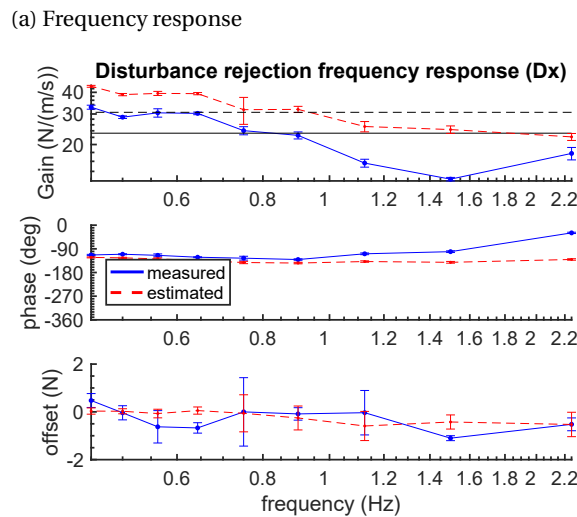
steps and not with a single frequency sweep. However, no conclusive reason is found yet why this pattern emerges.

The estimation error (Fig. 5.5c) in x-direction stays below 3-6 N for the RMS and peak error respectively. In y-direction, both errors stay around 10 N, caused by a force estimation bias. The estimation error in z-direction stays below 16-20 N for the RMS and peak error respectively.

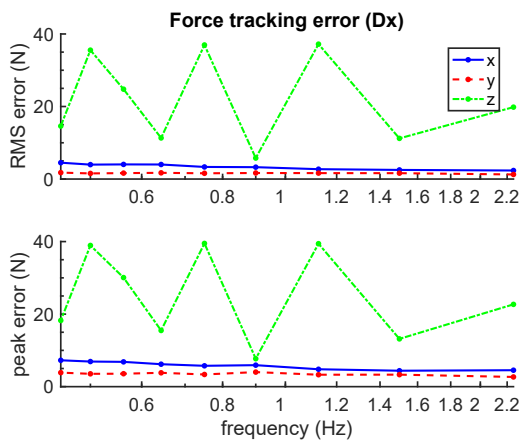
Non-nominal cases: Figure C.4 shows the non-nominal responses for a single frequency point. A lower BWU shows a lower gain and lower estimation errors in all directions. The introduction of a force bias in x-direction shows a slightly higher gain. Increasing the strap length shows lower y-estimation errors (not shown), which could be coincidental. The edge location shows similar performance. The low location shows a lower gain. Also, the estimation and tracking error in z-direction are lower, which could be coincidental.

5.5.2. Disturbance rejection performance: y-direction

The frequency response of the disturbance rejection experiment in y-direction (Fig. 5.6a) shows a difference between the measured and estimated responses. Also, large standard deviations are observed, most likely due to the observed instabilities during this experiment. For the estimated frequency response, the gain stays



(b) Tracking error



(c) Estimation error

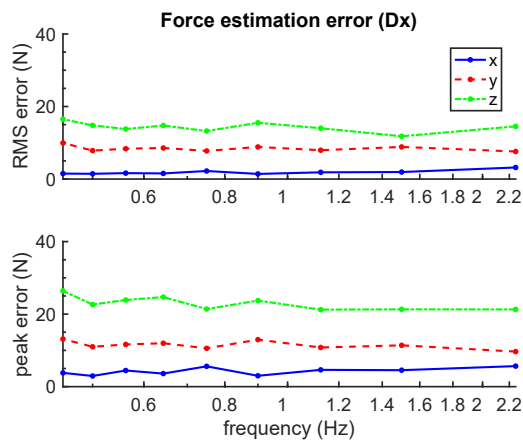


Figure 5.5: Results for the disturbance rejection experiment, x-direction. (a) shows the frequency response of the measured and estimated forces. The markers indicate the measurement points. The black lines indicate the half-power limit. The offset shows the force offset of the sine-fit. (b)/(c) show the tracking and estimation errors (RMS and peak) in all three directions. The dashed lines indicate the direction not perturbed.

around the same value for the entire frequency range and does not drop. For the measured frequency response, the gain is slightly higher. Also, the offset is around 5 N, whereas the estimated response shows an offset close to zero.

The tracking error (Fig. 5.6b) in y-direction is constant for the range of frequencies, with 5-10 N for RMS and peak error respectively. The tracking error in x-direction stays below 2-6 N for these errors. For the z-direction, the tracking errors increase when instabilities occur. These errors are of similar magnitudes as the observed tracking errors in the disturbance rejection experiment in x-direction.

The estimation error (Fig. 5.6c) in y-direction increases dramatically over the range of frequencies: from 10-20 N to 15-50 N, for RMS and peak error respectively. This is most likely due to the observed instabilities at higher frequencies. The estimation error in x-direction remains constant over the range of frequencies, with 6-10 N for the respective errors. The estimation error in z-direction also remains quite constant, with 15-22 N for the respective errors.

Non-nominal case:

Figure C.5 shows the non-nominal response for a single frequency point. Here, only the lower BWU case was performed, as the other cases showed unstable behaviour. The lower BWU case shows a lower gain and lower estimation errors, similar to what was observed in the x-direction, low BWU case.

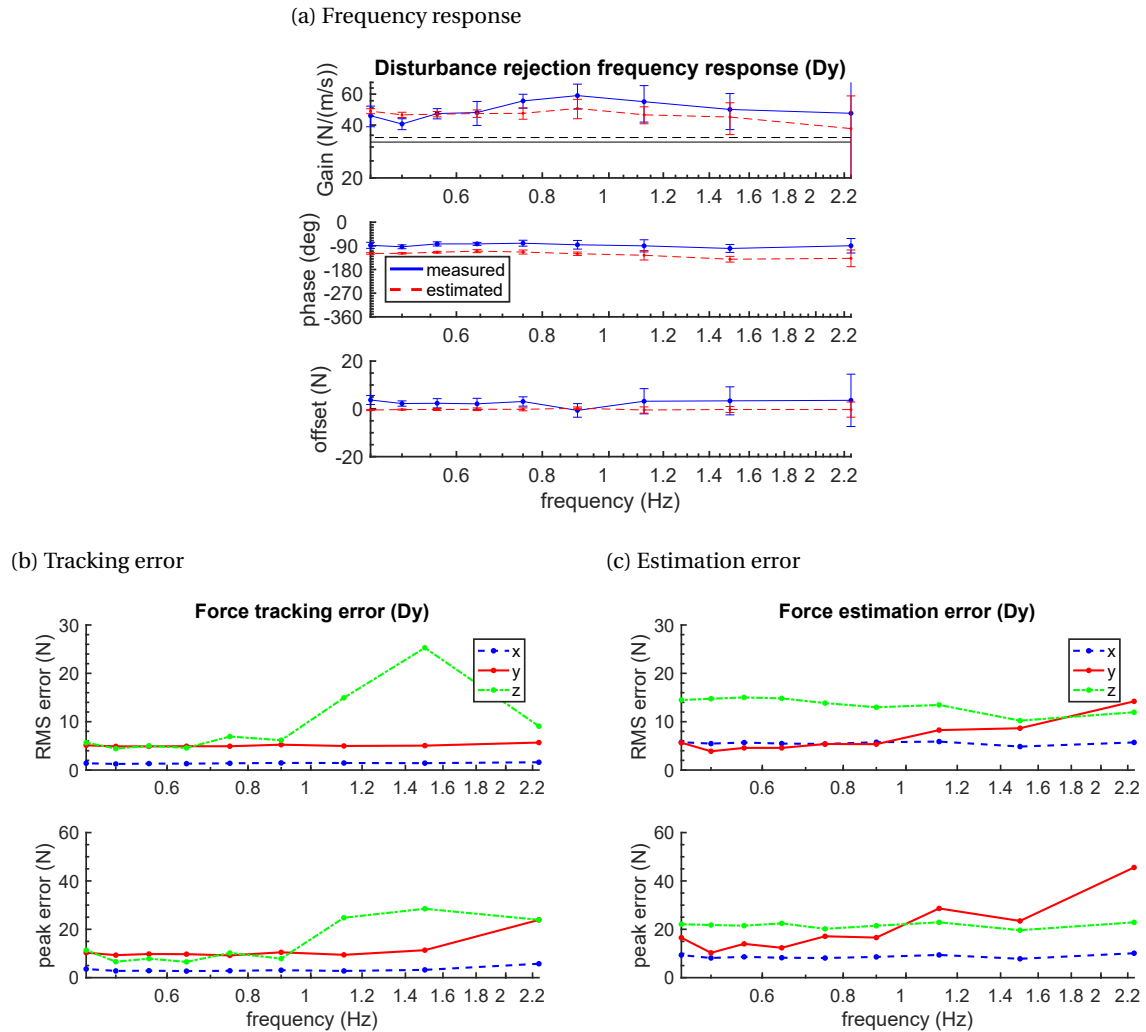


Figure 5.6: Results for the disturbance rejection experiment, y-direction. (a) shows the frequency response of the measured and estimated forces. The markers indicate the measurement points. The black lines indicate the half-power limit. The offset shows the force offset of the sine-fit. (b)/(c) show the tracking and estimation errors (RMS and peak) in all three directions. The dashed lines indicate the direction not perturbed.

5.5.3. Disturbance rejection performance: z-direction

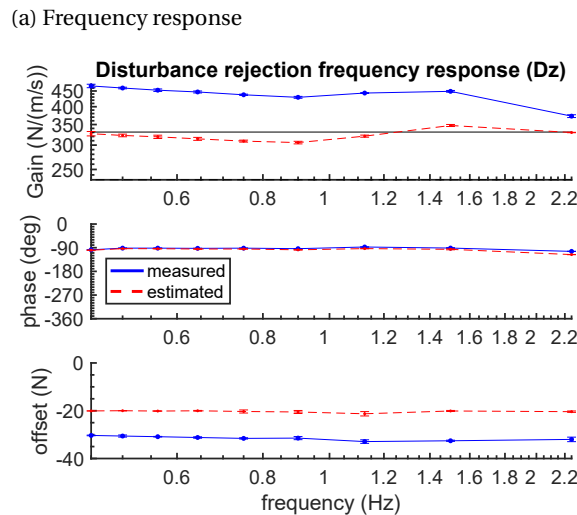
The frequency response of the disturbance rejection experiment in z-direction (Fig. 5.7a) shows that the gain remains relatively constant over the range of frequencies. Again, there is a notable difference between the estimated and measured frequency response. The offset shows that there is a constant bias of 20 N that the RYSEN measures and another 10 N offset between the estimated and measured responses. The standard deviation is low, meaning that the behaviour to vertical disturbances has a low variability.

For the tracking errors (Fig. 5.7b) it shows that errors in z-direction go up to 40-80 N for the RMS and peak error respectively. The tracking error in x- and y-direction are of similar magnitude and constant with 2-5 N for the RMS and peak error respectively.

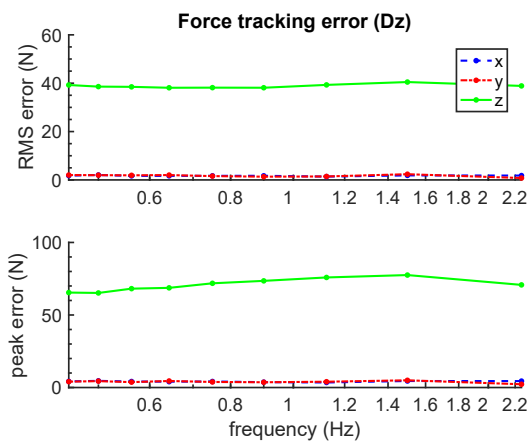
For the estimation errors (Fig. 5.7c), the peak errors in z-direction increases slightly with the frequency from

30-43 N, whereas the RMS error stays constant over the range of frequencies with 20 N. The estimation error in y-direction is 10-15 N for the RMS and peak error respectively, whereas x-directions these errors are only 2-5 N.

Non-nominal cases: Figure C.6 shows the non-nominal responses for a single frequency point. The low BWU and edge location have no notable influence on the performance. Increasing the strap length slightly decreases the gain, whereas the lower location increases the gain. This seems to agree with the assumption that changes in the stiffness matrix change the performance, introduced in 3. However, more experiments are needed to prove this.



(b) Tracking error



(c) Estimation error

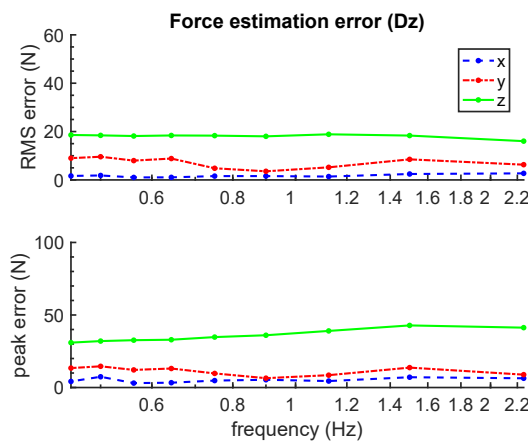


Figure 5.7: Results for the disturbance rejection experiment, z-direction. (a) shows the frequency response of the measured and estimated forces. The markers indicate the measurement points. The black lines indicate the half-power limit. The offset shows the force offset of the sine-fit. (b)/(c) show the tracking and estimation errors (RMS and peak) in all three directions. The dashed lines indicate the direction not perturbed.

5.6. Nominal cases: overview

Table 5.3 shows the main findings of the nominal dynamic experiments. Note that for the tracking and estimation error, the mean and maximum RMS errors, over the range of frequencies, are shown. The results show, for both experiments, RMS tracking errors up to 10-20 N for the x- and y-direction and up to 40 N for the z-direction. These are errors that the RYSEN measures. For the estimation errors, taking the maximum RMS error over the frequency range, errors go up to 20, 25 and 25 N for the x-, y- and z-direction respectively. This estimation error is an additional uncertainty on the output force.

For the force output experiment, the half-power bandwidth is 2.3-1.3 Hz for the x- and y direction and 1.2 Hz for the z-direction. The maximum offset, given with the measured forces, goes up to 10, 15, 40 N for the x-, y- and z-direction respectively. For the disturbance rejection experiment, the half-power bandwidth was only observed in x-direction with 0.9 Hz. The maximum offset is below 5 N for the x- and y direction and below 35 N for the z-direction.

Table 5.3: Result overview of the force output experiment (F-i) and disturbance rejection experiment (D-i), for direction i. The tracking error, bandwidth and offset uses the forces estimated by the RYSEN. Please note that the offset(*) is given with the measured forces and not the estimated forces.

Overview of experiments:		F-x	F-y	F-z	D-x	D-y	D-z
ϵ_t - RMS - x (N)	Mean	10.35	2.96	0.52	3.42	1.41	1.73
	Max	17.62	5.26	1.24	4.51	1.61	2.03
ϵ_t - RMS - y (N)	Mean	0.92	8.09	1.60	1.60	5.08	1.71
	Max	2.02	10.41	1.93	1.77	5.69	2.37
ϵ_t - RMS - z (N)	Mean	29.92	20.53	27.13	21.92	9.12	38.82
	Max	37.13	37.13	31.93	37.20	25.28	40.48
ϵ_{est} - RMS - x (N)	Mean	6.65	4.43	0.44	1.86	5.56	1.70
	Max	19.65	7.48	0.93	13.11	22.49	2.72
ϵ_{est} - RMS - y (N)	Mean	1.49	13.58	11.11	8.42	6.73	7.09
	Max	3.56	25.29	13.11	9.96	14.21	9.59
ϵ_{est} - RMS - z (N)	Mean	16.82	15.11	13.96	14.33	13.50	18.13
	Max	20.19	18.26	22.49	16.51	15.02	18.86
Bandwidth (Hz)	Useful freq.	0.4	0.6	0.4	-	-	-
	Half-power	2.3	1.3	1.2	0.9	-	-
Offset (N)*	Mean abs.	2.28	5.34	32.80	0.40	2.70	31.50
	Max abs.	10.62	15.41	38.61	1.10	3.71	32.91

5.7. Non-nominal cases: overview

The limited number of non-nominal tests and the presence of estimation errors make it difficult to have strong conclusions on the influence of configuration on performance. Initial hypotheses are given: First, a lower BWU seems to lower the estimation and tracking errors. Also for the disturbance rejection experiments it seems to lower the gain. This could be explained by the observations made in Section 3.5.4.

Second, the edge location and introduction of force bias does not seem to notably change performance. Chapter 3 showed that the unloading force and horizontal location indeed have a smaller influence on the stiffness matrix. Finally, the described influences of vertical location could also be explained by Section 3.2.2. The influence of the high (straps) and low location on the stiffness matrix seems to be present, but any conclusions on it might be premature.

5.8. Discussion

5.8.1. Dominant behaviour

The results indicate that the estimation error was dominant to the performance limitations of the RYSEN. The analyses used in previous chapters assumed a static model, rather than a model with sensing and actuation. These analyses gave an indication on configurations that could affect the performance. However, the effect of the configuration tends to be smaller than the uncertainty of the force estimation. Depending on the number of possible configurations, it might have been easier to perform pilot studies rather than doing similar analyses.

5.8.2. Test improvements

Future tests could be improved with several alterations. First, introducing damping to the endpoint of the test setup might imitate the conditions of human testing more and alleviate the instability problems that occurred. With human testing the instabilities in y-direction are also observed, but smaller than when using

this stiff test setup. Also, the ball-joint and rod will be replaced by a square tube with a fixed endpoint, as it more closely resembles the connection to the body.

Finally, the force output tests seem to be useful to capture the behaviour of the RYSEN. However, it is suggested that the disturbance rejection tests could be designed for faster walking subjects (1.6 m s^{-1}), meaning higher frequencies. Increasing the BWU can also amplify the effect of disturbances, which allows the RYSEN to demonstrate how it will mitigate those larger disturbances.

5.9. Conclusion

The force bandwidth was determined and lower than expected by the developers, which was 5 Hz for the lateral directions and 2 Hz for the vertical direction. However, these bandwidth requirements were chosen as best-possible-outcomes. Using the estimated frequency responses, the force output half-power bandwidth is 2.3-1.3 Hz for the x- and y direction and 1.2 Hz for the z-direction. Disturbance rejection seems sufficient in x-direction, but not in y-direction (unstable) and z-direction (too low control gains).

The force estimation error is expected to be the main limitation of the performance. Simply said, the RYSEN 'thinks' it performs better than the measured results indicate. The force estimations of y- and z-direction seem the most problematic.

The tracking error in z-direction is not completely explained by the estimation error. It is assumed that the force tracking in z-direction can be improved by increasing the control gains.

Unstable behaviour was observed for the tests in y-direction, which can be partly explained with the use of a stiff test setup, instead of a human subject with lower stiffness and higher damping characteristics. Methods of improving the tests were given in the discussion.

6

Summary of discussions

6.1. Overview

This chapter summarizes the discussions presented in the previous chapters. Here, the limitations and improvements of the analytical and experimental methods are discussed. It also states the contribution of this work to the field of performance evaluation of BWS systems.

6.2. Analytical methods

Limitations and improvements on the analytical methods from Chapter 2 and 3 are given: First, a static model representing the RYSEN was used for the analyses. This approach allows for a simplified, yet thorough evaluation. However, the results from Chapter 5 show that the influence of force estimation in the RYSEN is high, which was not included in the chosen model. The model could be extended to include motor dynamics, sensing limitations and other non-linear characteristics. However, such extensions would increase the complexity of the model and results. It is unsure if this additional complexity would add to the conclusions that were derived with the simplified model.

The presented analytical methods from Chapters 2 and 3 are a useful tool that derived the experimental methods in Chapter 4. However, the current performance did not allow to prove that the conclusions from the analyses are valid for actuated systems. For this version of the RYSEN, the influence of configuration is less present than the sensing and control errors. In other words: You can show the performance of the RYSEN with these experiments, but you cannot prove the methods of non-linearity and configuration sensitivity with these experiments yet. However, initial results of the non-nominal cases do indicate the expected influence of the location and unloading force, based on the stiffness matrix (Sec. 3.2.2) and connection to the harness (Sec. 3.5.4).

The maximum absolute and relative linearization errors (Chapter 2) are chosen as the uncertainty range of testing for one direction at a time and adding responses. This is valid for static systems, but also a conservative measure. This is conservative because the maximum combination of disturbances are used, for a static model without any presence of force modulation. Furthermore, the relative linearization error increases when lower forces are reached. This makes it a difficult metric to interpret without the absolute linearization error and vice versa. Therefore the combination of both metrics gave a proper overview of the linearization error.

The sensitivity analysis (Chapter 3) was shown to be a useful tool for determining the most important configurations. The results depend on the chosen method (LSA versus GSA), range (top, bottom, complete) and weight factors on the stiffness matrix. Variance-based sensitivity analysis allowed for a complete overview of sensitivity and interaction between configuration parameters. However, this 'black-box' approach might require prior knowledge to be interpreted correctly.

6.3. Experimental methods

In general, the experimental methods were deemed well-chosen and showcased the performance and limitations of the RYSEN for a set of realistic forces and disturbances. The influence of BWU (in the centre) and z-location (along the workspace) are the most interesting configurations to test more thoroughly. This was also suggested by the analyses of Chapter 3.

Future tests can be improved based on the results and observations, as described in Section 5.8.2. These improvements include adding damping to the endpoint and increasing the frequency of perturbation based on normal walking, instead of slower walking speeds.

Other tests could be added to show performance characteristics. First, for the disturbance rejection test, a fixed disturbance amplitude and continuously increasing frequency can show when the system becomes unstable or when its errors would be unacceptable. This additional test does not allow for conventional system identification, but does show the limits of performance. Similar tests were done by Hidler et al. [13] with the ZeroG. Second, the evaluation can be performed with subjects, similar to Vallery et al. [19] for the FLOAT. However, only forces estimated by the RYSEN can be measured. The current version of the RYSEN shows substantial force estimation errors, making the results of subject testing less accurate.

6.4. Contributions to the field of performance evaluation

This work provided the following contributions to the field of performance evaluation of body weight support systems or, more generally, of suspended cable-driven parallel mechanisms implementing force control.

First, analytical methods and metrics were derived to determine the required directions and configurations for performance evaluation. Other systems can use the same methods and metrics to derive similar suggestions for experimental design. The analyses give a conservative metric for non-linearity, based on static spring systems subjected to realistic disturbances based on human walking. The analyses also give a metric for sensitivity of configurations on system characteristics.

Second, the experimental methods can directly be implemented for other cable-driven BWS systems. The types of experiments, metrics, input signals, test setup and visualization of results are derived based on human walking and support strategies. Only the chosen configurations are typical for 3D overground BWS systems and based on the results of Chapter 3. The experiments are based on three modes of operation: static force tracking, dynamic force tracking and disturbance rejection or zero-impedance mode.

Finally, the reconfigurable test setup that was developed allows for objective performance evaluation and system identification. The setup makes use of an external sensor and has the option to give a sinusoidal disturbance with an amplitude range of 0.01 to 0.05 m. This setup requires no costly linear actuators, as was observed in other studies [13, 14]. Other human-machine interfaces using force control can use this setup for systematic performance evaluation.

7

Conclusions

The following potential challenges were identified for the performance evaluation of body weight support systems: (1) exciting the system in one direction at a time, (2) configuration selection and (3) visualization of results.

First, a metric of non-linearity was proposed and applied for non-linear static spring models, representing body weight support systems. This showed that a 2D simplified RYSEN model has a maximum absolute linearization error of 11 N and a maximum relative linearization error of 3 % for the range of configurations and disturbances. These metrics can be taken as uncertainty ranges when adding system responses from testing in one direction at a time.

Second, methods were proposed to derive the most important configurations for performance evaluation. Variance-based sensitivity analysis was applied to a weighted stiffness matrix where the weight factors are based on the disturbing moment around the base of support. This method indicates that the vertical location changes the behaviour of the simplified RYSEN model more than the horizontal location. It also showed that the influence of unloading force changed the output behaviour, but this only needs to be assessed in one location of the workspace.

Experimental methods are proposed to assess the performance of the RYSEN. These methods are based on human walking and support strategies and can be applied to any overground BWS system. Three experiments and their respective input signals were derived: static force tracking, force output tracking and disturbance rejection. The frequency response (gain, phase, offset), tracking and estimation errors were chosen as output metrics. A test setup was developed to objectively obtain these metrics for relevant input signals. The proposed experiments and test setup were able to characterize the RYSEN.

The performance of the RYSEN shows that the force output bandwidth is 2.3-1.3 Hz for the x- and y-direction and 1.2 Hz for the z-direction, using the estimated forces of the RYSEN. For the disturbance rejection experiment it showed better performance in x-direction than in z-direction. Disturbing the system in y-direction often resulted in unstable behaviour when using this test setup. The force estimation is seen as the main limitation of performance. Taking the maximum RMS error over the frequency range gave estimation errors up to 20, 25 and 25 N for the x-, y- and z-direction respectively.

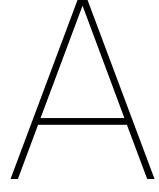
The results of the RYSEN did not allow to prove the influence of (1) system non-linearity and (2) configuration selection yet, as the force estimation error was dominant in output behaviour. The influence of non-nominal configurations did seem to agree with prior analyses, but more testing is required with future versions of the RYSEN.

Future work includes improving the experimental methods by increasing the speed of disturbance and making minor physical alterations to the test setup. These improvements will be implemented and tested with a new version of the RYSEN that has improved sensing and control performance.

Bibliography

- [1] H. Barbeau and M. Visintin, "Optimal outcomes obtained with body-weight support combined with treadmill training in stroke subjects," *Archives of Physical Medicine and Rehabilitation*, vol. 84, pp. 1458–1465, oct 2003.
- [2] P. W. Duncan, K. J. Sullivan, A. L. Behrman, S. P. Azen, S. S. Wu, S. E. Nadeau, B. H. Dobkin, D. K. Rose, J. K. Tilson, S. Cen, and S. K. Hayden, "Body-weight-supported treadmill rehabilitation after stroke," *New England Journal of Medicine*, vol. 364, pp. 2026–2036, may 2011.
- [3] L. M. Giangregorio, A. L. Hicks, C. E. Webber, S. M. Phillips, B. C. Craven, J. M. Bugaresti, and N. McCartney, "Body weight supported treadmill training in acute spinal cord injury: impact on muscle and bone," *Spinal Cord*, vol. 43, pp. 649–657, jun 2005.
- [4] J.-B. Mignardot, C. G. L. Goff, R. van den Brand, M. Capogrosso, N. Fumeaux, H. Vallery, S. Anil, J. Lanini, I. Fodor, G. Eberle, A. Ijspeert, B. Schurch, A. Curt, S. Carda, J. Bloch, J. von Zitzewitz, and G. Courtine, "A multidirectional gravity-assist algorithm that enhances locomotor control in patients with stroke or spinal cord injury," *Science Translational Medicine*, vol. 9, p. eaah3621, jul 2017.
- [5] P. O. Riley, G. Paolini, U. D. Croce, K. W. Paylo, and D. C. Kerrigan, "A kinematic and kinetic comparison of overground and treadmill walking in healthy subjects," *Gait & Posture*, vol. 26, pp. 17–24, jun 2007.
- [6] S. J. Lee and J. Hidler, "Biomechanics of overground vs. treadmill walking in healthy individuals," *Journal of Applied Physiology*, vol. 104, pp. 747–755, mar 2008.
- [7] M. Plooij, U. Keller, B. Sterke, S. Komi, H. Vallery, and J. von Zitzewitz, "Design of RYSEN: an intrinsically safe and low-power 3d overground body weight support," *IEEE Robotics and Automation Letters*, pp. 1–1, 2018.
- [8] C. Gosselin, "Cable-driven parallel mechanisms: state of the art and perspectives," *Mechanical Engineering Reviews*, vol. 1, no. 1, pp. DSM0004–DSM0004, 2014.
- [9] M. Luces, J. K. Mills, and B. Benhabib, "A review of redundant parallel kinematic mechanisms," *Journal of Intelligent & Robotic Systems*, oct 2016.
- [10] R. Peuchen, "Performance evaluation of cable-driven parallel mechanisms." Literature report - remains unpublished, July 2017.
- [11] P. Bosscher, *Disturbance Robustness Measures and Wrench-Feasible Workspace Generation Techniques for Cable-Driven Robots*. PhD thesis, Georgia Institute of Technology, 2004.
- [12] R. Verhoeven, *Analysis of the Workspace of Tendon-based Stewart Platforms*. PhD thesis, Universität Duisburg-Essen, 2004.
- [13] J. Hidler, D. Brennan, iian Black, D. Nichols, K. Brady, and T. Nef, "ZeroG: Overground gait and balance training system," *The Journal of Rehabilitation Research and Development*, vol. 48, no. 4, p. 287, 2011.
- [14] M. Bannwart, M. Bolliger, P. Lutz, M. Gantner, and G. Rauter, "Systematic analysis of transparency in the gait rehabilitation device the FLOAT," in *2016 14th International Conference on Control, Automation, Robotics and Vision (ICARCV)*, IEEE, nov 2016.
- [15] S. A. Gard, S. C. Miff, and A. D. Kuo, "Comparison of kinematic and kinetic methods for computing the vertical motion of the body center of mass during walking," *Human Movement Science*, vol. 22, pp. 597–610, apr 2004.
- [16] M. S. Orendurff, A. D. Segal, G. K. Klute, J. S. Berge, E. S. Rohr, and N. J. Kadel, "The effect of walking speed on center of mass displacement," *The Journal of Rehabilitation Research and Development*, vol. 41, no. 6, p. 829, 2004.

- [17] W. Kraus, *Force Control of Cable-Driven Parallel Robots*. PhD thesis, Universität Stuttgart, 2015.
- [18] H. Vallery, A. Duschau-Wicke, and R. Riener, "Optimized passive dynamics improve transparency of haptic devices," *Robotics and Automation, 2009. ICRA '09. IEEE International Conference*, May 2009.
- [19] H. Vallery, P. Lutz, J. von Zitzewitz, G. Rauter, M. Fritschi, C. Everarts, R. Ronsse, A. Curt, and M. Bolliger, "Multidirectional transparent support for overground gait training," in *Institute of Electrical and Electronics Engineers (IEEE)*, jun 2013.
- [20] S. Apte, M. Plooiij, and H. Vallery, "Influence of body-weight unloading on human gait characteristics: a review." in review, 2017.
- [21] J. Molenbroek, "Dined - anthropometry," Dec. 2017.
- [22] A. Saltelli, M. Ratto, T. Andres, F. Campolongo, J. Cariboni, D. Gatelli, M. Saisana, and S. Tarantola, *Global Sensitivity Analysis. The Primer*. John Wiley & Sons, Ltd, dec 2007.
- [23] B. Iooss and P. Lemaître, "A review on global sensitivity analysis methods," in *Uncertainty Management in Simulation-Optimization of Complex Systems*, pp. 101–122, Springer US, 2015.
- [24] I. Sobolj, "Global sensitivity indices for nonlinear mathematical models and their monte carlo estimates," *Mathematics and Computers in Simulation*, vol. 55, pp. 271–280, feb 2001.
- [25] A. Saltelli, P. Annoni, I. Azzini, F. Campolongo, M. Ratto, and S. Tarantola, "Variance based sensitivity analysis of model output. design and estimator for the total sensitivity index," *Computer Physics Communications*, vol. 181, pp. 259–270, feb 2010.
- [26] T. Homma and A. Saltelli, "Importance measures in global sensitivity analysis of nonlinear models," *Reliability Engineering & System Safety*, vol. 52, pp. 1–17, apr 1996.
- [27] F. Cannavó, "Sensitivity analysis for volcanic source modeling quality assessment and model selection," *Computers & Geosciences*, vol. 44, pp. 52–59, jul 2012.
- [28] F. Pianosi, F. Sarrazin, and T. Wagener, "A matlab toolbox for global sensitivity analysis," *Environmental Modelling & Software*, vol. 70, pp. 80–85, aug 2015.
- [29] F. Parietti, G. Baud-Bovy, E. Gatti, R. Riener, L. Guzzella, and H. Vallery, "Series viscoelastic actuators can match human force perception," *IEEE/ASME Transactions on Mechatronics*, vol. 16, pp. 853–860, oct 2011.
- [30] E. K. Antonsson and R. W. Mann, "The frequency content of gait," *Journal of Biomechanics*, vol. 18, pp. 39–47, jan 1985.
- [31] C. Angeloni, P. Riley, and D. Krebs, "Frequency content of whole body gait kinematic data," *IEEE Transactions on Rehabilitation Engineering*, vol. 2, pp. 40–46, mar 1994.
- [32] E. Samur, *Performance Metrics for Haptic Interfaces*. Springer London, 2012.



Appendix: Variance-based sensitivity analysis

The sensitivity indices from Chapter 3 are calculated as follows [25]: Given an output model $Y = f(X_1, X_2, \dots, X_k)$ with generic factor X_i has a first-order sensitivity index.

$$S_i = \frac{V_{X_i}(E_{\mathbf{X}_{-i}}(Y|X_i))}{V(Y)} \quad (\text{A.1})$$

$$V(Y) = V_{X_i}(E_{\mathbf{X}_{-i}}(Y|X_i)) + E_{X_i}(V_{\mathbf{X}_{-i}}(Y|X_i)) \quad (\text{A.2})$$

where $V_{X_i}(\cdot)$ takes the variances of argument (\cdot) over X_i , $E_{X_i}(\cdot)$ takes the mean of argument (\cdot) over X_i , \mathbf{X}_{-i} denotes the matrix containing all factors except for X_i , finally $(Y|X_i)$ denotes the output function for which X_i is kept constant. For this denotation, the numerator contains the first order variance, ranging from 0 to $V(Y)$. This can be interpreted as the 'expected reduction that would be obtained if X_i would be fixed.' In the denominator you have the first order variance and the so-called residual. This shows the total variance when all factors X_i are varied over their respective range.

The total effect index is calculated as follows:

$$S_{T_i} = \frac{E_{\mathbf{X}_{-i}}(V_{X_i})(Y|\mathbf{X}_{-i})}{V(Y)} = 1 - \frac{V_{\mathbf{X}_{-i}}(E_{X_i}(Y|\mathbf{X}_{-i}))}{V(Y)} \quad (\text{A.3})$$

here the numerator $V_{\mathbf{X}_{-i}}(E_{X_i}(Y|\mathbf{X}_{-i}))$ gives the first order variance of all factors except for X_i , which is subtracted from the total possible variance. Numerical estimators are used to calculate the expressions in equation A.1 and A.3 based on best case practices for efficiency and accuracy. In the toolbox of Cannavo [27] the estimators of Saltelli et al. [25] are used:

$$V_{X_i}(E_{\mathbf{X}_{-i}}(Y|X_i)) \approx \frac{1}{N} \sum_{j=1}^N f(\mathbf{B})_j (f(\mathbf{A}_{\mathbf{B}}^{(i)})_j - f(\mathbf{A})_j) \quad (\text{A.4})$$

$$E_{\mathbf{X}_{-i}}(V_{X_i})(Y|\mathbf{X}_{-i}) \approx \frac{1}{2N} \sum_{j=1}^N (f(\mathbf{A})_j - f(\mathbf{A}_{\mathbf{B}}^{(i)})_j)^2 \quad (\text{A.5})$$

This consist of two sets of matrices (\mathbf{A}, \mathbf{B}) with N quasi-random samples of $i = 1 \dots k$ parameters. Matrix $\mathbf{A}_{\mathbf{B}}^{(i)}$ consist of matrix \mathbf{A} where column i is replaced by column i of matrix \mathbf{B} .

B

Appendix: Test protocol

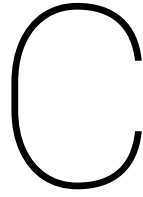
B.1. Protocol and safety during the experiments

B.1.1. Protocol

- Put setup in desired configuration
 - Position the RYSEN to fit the straps to the test setup
 - Select desired unloading force - force control mode
 - Check location of RYSEN again
 - If needed, winch the spring to its desired length, such that it counteracts the unloading force
- Safety check
 - Device in position
 - Force control mode on
 - Correct experiment selected
 - Ready to capture data
- Start capturing sensor and RYSEN data
- Wait 5 seconds for static force measurement
- Start step-wise perturbation protocol
- End protocol or hit emergency button
- Stop capturing RYSEN data
- Save captured data
- Repeat in new configuration, direction or disturbance set

B.1.2. Checks in-between tests

- Check if setup moved
- Check the strap length
- Check for slip in motor coupling
- Check if all data is collected

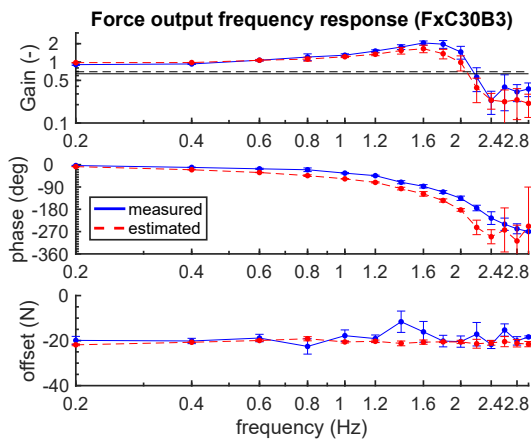


Appendix: Additional figures

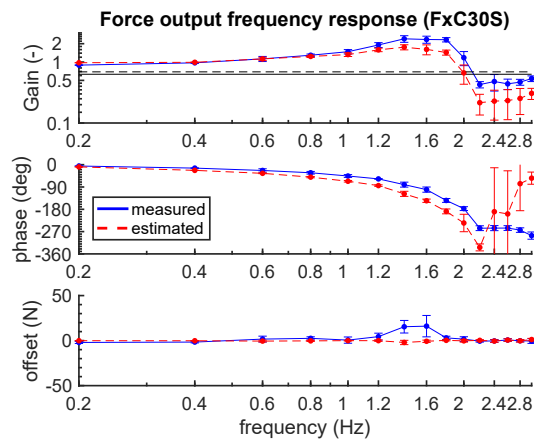
C.1. Force output experiment: non-nominal cases

x-direction:

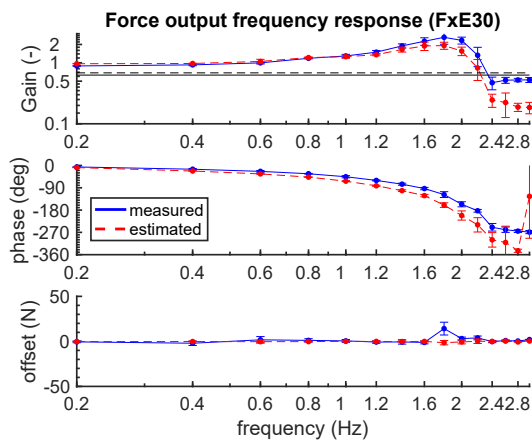
(a) Bias force



(b) Strap length increase



(c) Edge location



(d) Low location

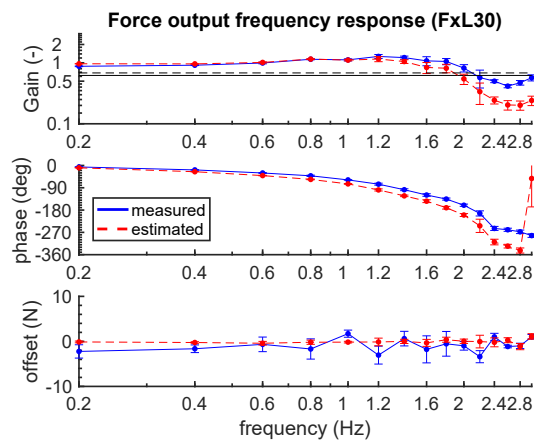
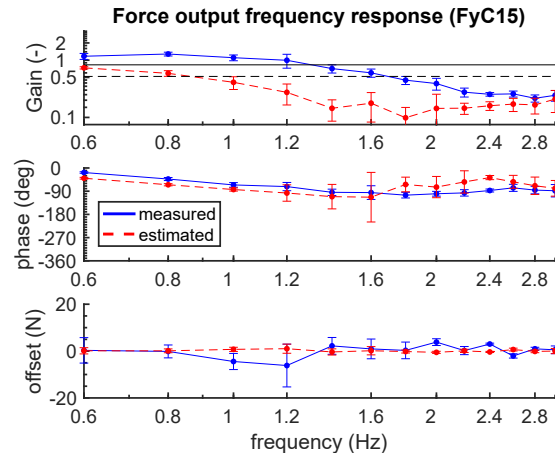


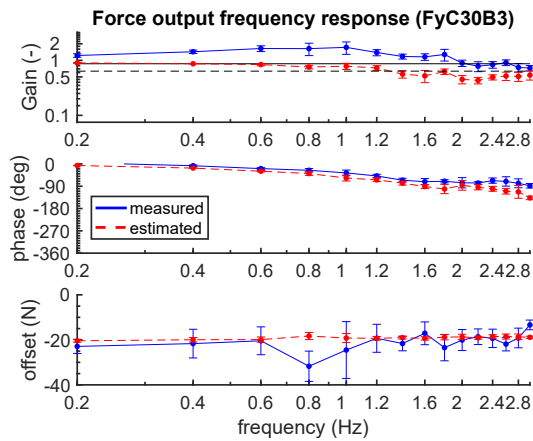
Figure C.1: Results for the force output experiment, x-direction non-nominal cases. The figures show the frequency responses of the measured and estimated forces. The markers indicate the measurement points. The black lines indicate the half-power limit. The offset shows the force offset of the sine-fit.

y-direction:

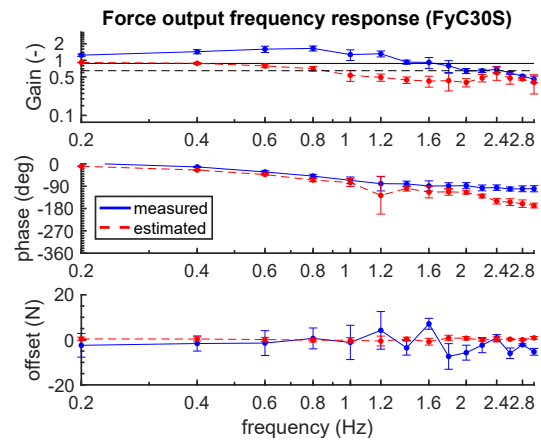
(a) Low body weight unloading



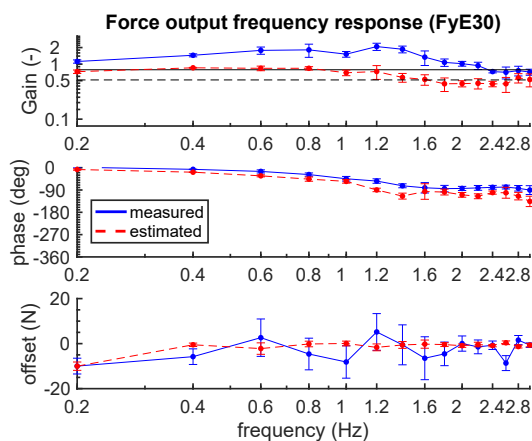
(b) Bias force



(c) Strap length increase



(d) Edge location



(e) Low location

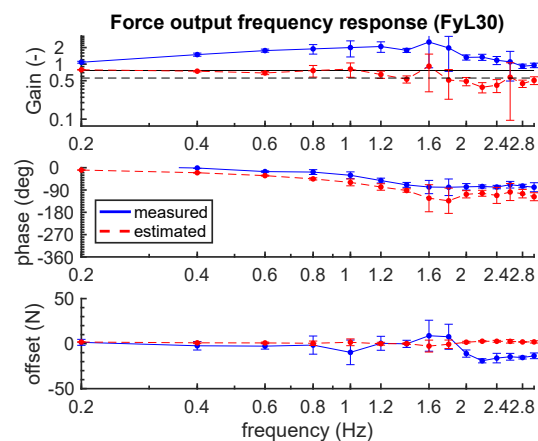
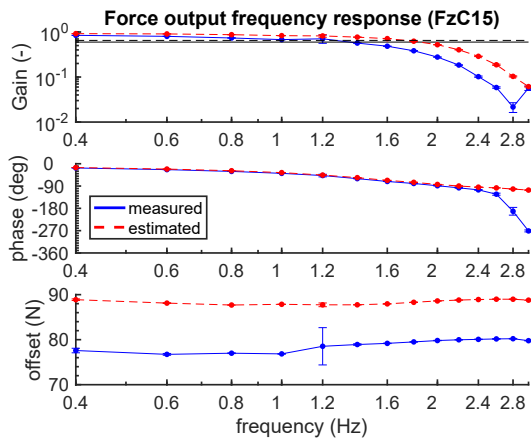


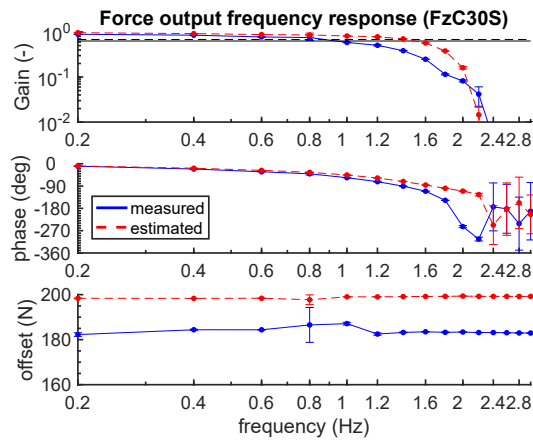
Figure C.2: Results for the force output experiment, y-direction non-nominal cases. The figures show the frequency responses of the measured and estimated forces. The markers indicate the measurement points. The black lines indicate the half-power limit. The offset shows the force offset of the sine-fit.

z-direction:

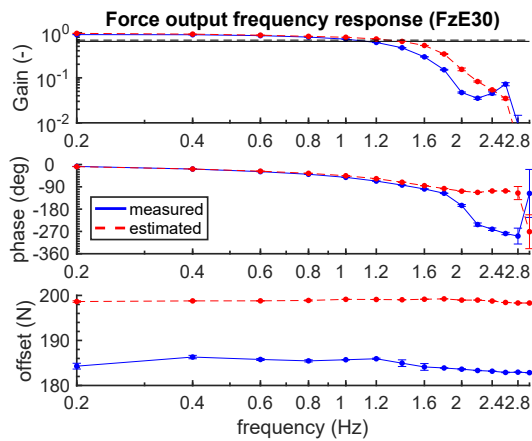
(a) Low body weight unloading



(b) Strap length increase



(c) Edge location



(d) Low location

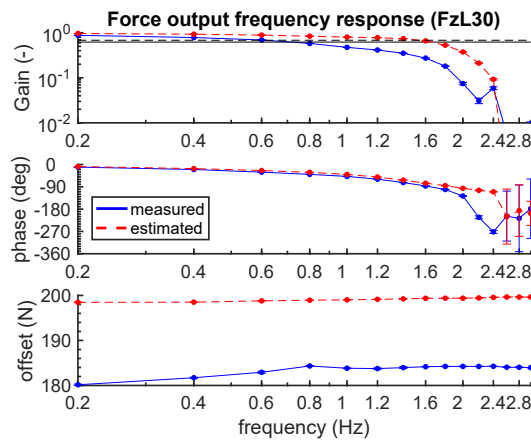


Figure C.3: Results for the force output experiment, z-direction non-nominal cases. The figures show the frequency responses of the measured and estimated forces. The markers indicate the measurement points. The black lines indicate the half-power limit. The offset shows the force offset of the sine-fit.

C.2. Disturbance rejection experiment: non-nominal cases

x-direction:

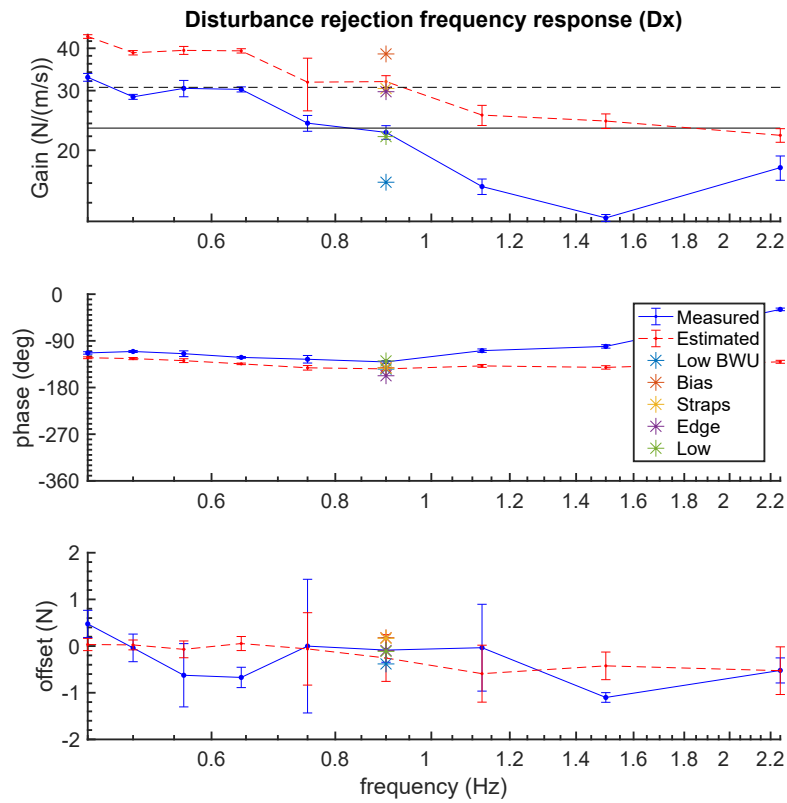


Figure C.4: Results for the disturbance rejection experiment in x-direction with non-nominal cases. The figures show the nominal frequency response together with the non-nominal cases measured in a single point. The dot markers indicate the measurement points of the nominal cases. The stars indicate the respective non-nominal cases. The black lines indicate the half-power limit. The offset shows the force offset of the sine-fit.

y-direction:

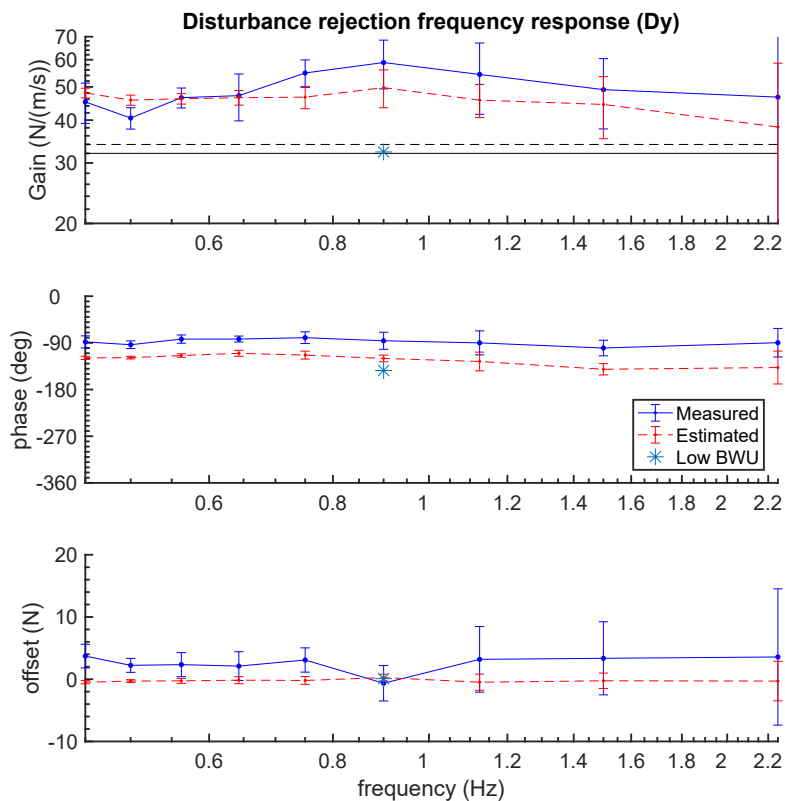


Figure C.5: Results for the disturbance rejection experiment in y-direction with non-nominal cases. The figures show the nominal frequency response together with the non-nominal cases measured in a single point. The dot markers indicate the measurement points of the nominal cases. The stars indicate the respective non-nominal cases. The black lines indicate the half-power limit. The offset shows the force offset of the sine-fit.

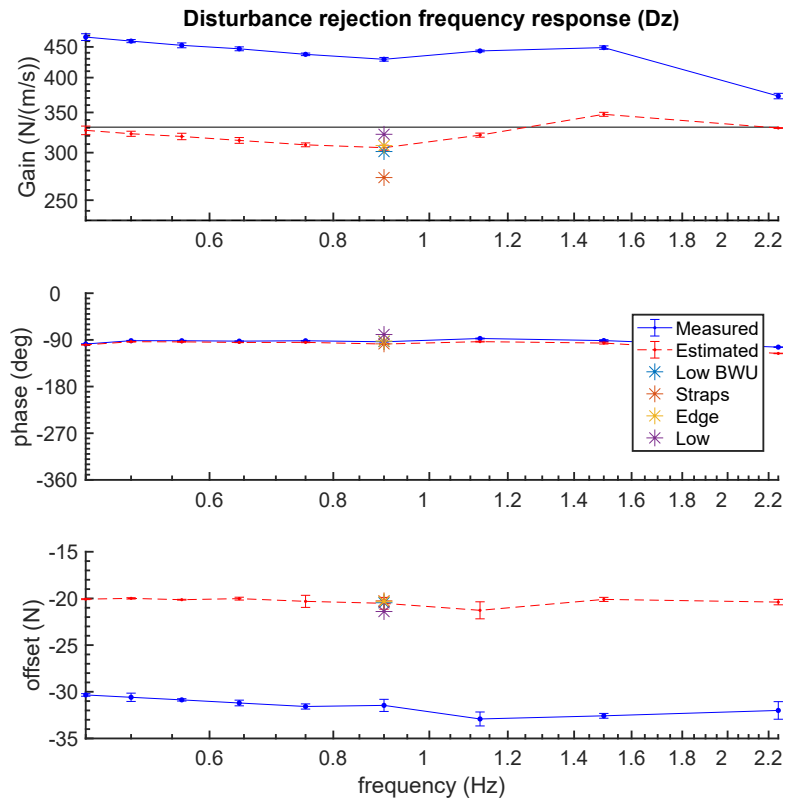
z-direction:

Figure C.6: Results for the disturbance rejection experiment in z-direction with non-nominal cases. The figures show the nominal frequency response together with the non-nominal cases measured in a single point. The dot markers indicate the measurement points of the nominal cases. The stars indicate the respective non-nominal cases. The black lines indicate the half-power limit. The offset shows the force offset of the sine-fit.